Spring 5-2020

Vehicle Design Study of a Straight Flying-Wing with Bell-Shaped Spanload

Kevin Hainline
Washington University in St. Louis

Washington University in St. Louis

James McKelvey School of Engineering

Department of Mechanical Engineering and Material Science

Thesis Examination Committee:
Ramesh K. Agarwal, Chair
Kevin A. Wise
David A. Peters

Vehicle Design Study of a Straight Flying-Wing with Bell-Shaped Spanload

by

Kevin Hainline

A thesis presented to
the James McKelvey School of Engineering
of Washington University in partial fulfillment of the
requirements for the degree of Master of Science

May 2020
Saint Louis, Missouri

Contents

List of Figures . . . . . **iii**

List of Tables . . . . . **v**

Nomenclature . . . . . **vi**

Acknowledgments . . . . . **vii**

Abstract . . . . . **viii**

1 Introduction **1**
1.1 Motivation 1
1.2 Scope of The Thesis 2
1.3 Review of Literature 2
1.3.1 Avian Flight Research 2
1.3.2 Morphing Geometry 3
1.3.3 Optimal Spanloads 4

2 The Straight Flying-Wing **6**
2.1 Motivation 6
2.2 Biom Configuration Features 7
2.3 Design Risks 8
2.3.1 Longitudinal Dynamics 8
2.3.2 Lateral-Directional Control 9

3 Biom T1 - Vehicle Design **11**
3.1 Geometry Determination 13
3.1.1 Cosine Root Extension 14
3.1.2 Pure Bell Region 14
3.1.3 Linear Taper Region 15
3.1.4 Elliptical Taper Region 15
3.2 Comparison to Albatross 16
3.3 Thickness Profile 17
3.4 Aerodynamic Characteristics Over Span 19

4 Biom T1 - Stability and Control Analysis **23**

4.1 Stability - Linear Plant Characteristics . . . 23
4.2 Control . . . 25
4.2.1 Elevators . . . 26
4.2.2 Innerons and Outerons . . . 27
4.3 Optimizing Planform for Control Power . . . 30
4.4 Closed-Loop Control . . . 33
4.4.1 Longitudinal Control . . . 33
4.4.2 Lateral-Directional Control . . . 39
4.4.3 Outeron Schedule . . . 45

5 Biom T1 Flight Test Prototype . . . 47
5.1 Sideslip Measurement . . . 47
5.2 Guidance Laws . . . 52
5.3 VMS Development . . . 55

6 Application . . . 56
6.1 Stacking . . . 56
6.2 Survivability . . . 57
6.3 Performance . . . 58

7 Conclusions . . . 60

Appendix A Guidance Test Case Timehistories . . . 61

Appendix B High Level Block Diagrams . . . 63

Appendix C Linear Analysis Data . . . 67

References . . . 68

List of Figures

1.1 Comparison of Elliptic and Bell-Shaped Spanloads 5

2.1 Prandtl D glider model 6
2.2 Biom configuration overview 8
2.3 Lateral-Directional control space 10

3.1 Isometric view of the Biom T1 CAD model 11
3.2 Initial Bell-Planform 13
3.3 Biom planform sections 14
3.4 Geometry Buildup for Biom T1 15
3.5 Overlay of Biom-Para 17
3.6 Thickness profile, front view 18
3.7 Percentage thickness distribution along the span 18
3.8 Thickness distribution along the span due to various components 19
3.9 Assumed downwash and target Cl distribution along the span 20
3.10 Twist prediction 20
3.11 Calculated lift distribution comparison against the ideal lift distribution . . . 21
3.12 Lift distribution near stall 21
3.13 Lift coefficient distribution at cruise and near stall 21
3.14 Induced angle distribution at cruise 22
3.15 Induced and local drag distribution at cruise 22

4.1 Longitudinal Open-Loop Eigenvalues 24
4.2 Lateral-Directional Open-Loop Eigenvalues 25
4.3 Biom T1 with control surfaces defined in OpenVSP 26
4.4 Lift distribution in OpenVSP with different control deflections 27
4.5 Drag distribution in OpenVSP with different control deflections 27
4.6 Left wing drag with and without outeron deflection 28
4.7 Right wing drag with and without outeron deflection 28
4.8 Cn vs Cl plot for 2° outeron deflection for various aircraft 31
4.9 C_n vs. C_l with varying span fraction of the outeron at 2° deflection 32
4.10 System robustness to actuator dynamics 34
4.11 Acceleration timehistory step response 35
4.12 Robustness study - Nz time history step response 37
4.13 Longitudinal robustness study - root locus 38

4.14 Sideslip Timehistory Step Response 39
4.15 Robustness study - sideslip time history of step response 42
4.16 Lateral-directional robustness study - root locus 43
4.17 Lateral-directional robustness study - root locus, zoomed-in-view 44
4.18 Outeron schedule 45
4.19 Impact of outeron schedule on lift distribution 46

5.1 Traditional beta vane design [BasicAirData.eu(2014)]. 48
5.2 The 3D printed beta probe. (fingers are shown to describe the relative scale of the probe) 49
5.3 Wind tunnel setup for testing beta probe 50
5.4 Differential pressure for beta at probe angles -7 through 7 degrees 51
5.5 Overlaid pressure plots for beta probe measurements 51
5.6 Return to home guidance - actual guidance laws piloting a model of Biom T1 in a Simulink 6dof simulation 53

6.1 Survivable Biom geometry 58

A.1 General Signals 61
A.2 Trajectory Tracking 62
A.3 Trajectory Tracking Cont. 62

B.1 OFP Mode Logic 63
B.2 Longitudinal Control Law Implementation 64
B.3 Lateral-Directional Control Law Implementation 64
B.4 Mixer Implementation 65
B.5 Guidance Top-Level 65
B.6 Trajectory Determination 66
B.7 Trajectory Tracking 66

List of Tables

3.1 Wing geometry definition 12
3.2 Comparison of geometry parameters of albatross and Biom T1 16

4.1 Longitudinal Control Derivatives 26
4.2 Lateral-directional control derivatives 27
4.3 Longitudinal robustness variations 36
4.4 Variations in lateral-directional control to assess robustness 40

C.1 Full Table Data Longitudinal Robustness 67

Nomenclature

α_L	=	Local Angle of Attack
β	=	Angle of Sideslip
CL	=	Lift Coefficient of a Wing
Cp	=	Pressure Coefficient
c	=	Chord
b	=	Span
DP	=	Differential Pressure
δ_{xx}	=	Deflection of xx Control Surface
FADS	=	Flush Air-Data System
Λ	=	Sweep Angle
L	=	Lift
L'	=	Lift per Unit Span, or "Sectional Lift"
L'_0	=	Sectional Lift of the Root Chord
MAC	=	Mean Aerodynamic Chord
UAV	=	Unmanned Aerial Vehicle
Nz	=	Vertical Acceleration in the Body Frame
p	=	Roll Rate in the Body Frame
q	=	Pitch Rate in the Body Frame
r	=	Yaw Rate in the Body Frame
V_∞	=	Freestream Velocity
ω	=	Downwash
OFP	=	Operational Flight Program
VMS	=	Vehicle Management System

Acknowledgments

I would like to thank committee chair and thesis adviser, Dr. Ramesh Agarwal for his guidance and encouragement during the course of this investigation. I would also like to thank the thesis committee members Dr. Peters and Dr. Wise for their time and valuable input. Thanks to all the graduate and undergraduate students who took interest and contributed in this project and special thanks to undergraduate researcher, Jonathan Richter, for all his hard work.

Kevin Hainline

Washington University in Saint Louis
May 2020

ABSTRACT OF THE THESIS

Vehicle Design Study of a Straight Flying-Wing with Bell-Shaped Spanload

by

Kevin Hainline

Master of Science in Aerospace Engineering

Washington University in St. Louis, May 2020

Research Advisor: Professor Ramesh K. Agarwal

Straight flying-wing configurations, that is flying wings with zero quarter-chord sweep, are key to understanding bird flight, have potential performance improvements, and are suitable for "survivable" applications. Straight flying-wings are also well suited for morphing geometry, e.g. with variable twist, since changes in lift distribution do not impact longitudinal equilibrium. The straight-flying wing can adjust its lift distribution to optimize aerodynamic efficiency across a wide range of flight conditions. In this thesis, we conduct the design study of a flying-wing with bell-shaped spanload; the study vehicle is called "Biom T1". Biom T1 has a more efficient directional control scheme acheived by employing the same bell-shaped lift-distribution as used by birds which creates a downwash distribution favorable to proverse yaw in the outer portion of the wing. The flying qualities and control system robustness are demonstrated through linear analysis and it is shown that straight flying-wings are viable in terms of stability and control and are suitable for high-efficiency, low-payload-volume applications.

Chapter 1

Introduction

1.1 Motivation

The configuration under study is called "Biom", short for bio-mimetic, and this describes a large family of vehicles of which we will study one in greater detail: "Biom T1". The Biom configuration can be considered as a successor to bell-shaped-spanload studies conducted at NASA Armstrong by Al Bowers with the Prandtl-D aircraft, the most notable differences are a straight wing (zero sweep and zero dihedral), and three pairs of control surfaces instead of the Prandtl-D's one pair of elevons.

The single pair of elevons is able to fully control the Prandtl-D but this simple control scheme imposes limitations on on the shape of the tailless flying wing: dihedral and sweep are required with emphasis on the sweep.

Development of a new control scheme for complete lateral-directional controllability opens up the configuration for more variations that impact lateral-directional stability since lateral-directional dynamics can be stabilized through active control.

The key variation under study is the removal of sweep, which has benefits for performance, stacking (storage compactness), and survivability.

Thus the primary motivation of this research is in expanding the available design space of tailless flying wings, and examining a subset of that design space.

In the process of exploring this design space, this study inadvertently converges to an aerodynamic shape found in nature. This brings in secondary motivations of this research, namely the study of avian flight and applications of morphing aerodynamic geometry.

1.2 Scope of The Thesis

The vehicle design study utilizes a new aerodynamic control scheme to stabilize a vehicle with poor no-control dynamics. As a result, technical focus beyond configuration itself is split between aerodynamic control and flight control laws and only a cursory examination is given to each area in this research.

Aerodynamic control part will examine the nature of proverse yaw using a bell-shaped-spanload and conduct sensitivity studies to maximize the control power. Only control power at the cruise condition is considered and panel methods are used as the simplest and fastest tool to capture the aerodynamics.

It is surmised that the studied configuration is stabilizable through active control. Control law analysis will be used to substantiate this claim by demonstrating that the system is not only stabilizable but robust to aerodynamic stability and control uncertainties. Analysis will be strictly limited to linear analysis at a single flight condition.

1.3 Review of Literature

1.3.1 Avian Flight Research

Aircraft design has shifted away from its avian roots dating back to conceptual designs proposed by Leonardo Da-Vinci and Otto Lilienthal. Aircraft ranging from small unmanned aerial vehicles ($\sim$1m span) to enormous cargo jets ($\sim$60m span) have little in common with their biological counterparts. In the past two decades, enthusiasm for micro air vehicles has led to renewed interest in basic avian flight mechanics [Dvorak(2016)].

Birds achieve performance and efficiency gains by utilizing complex wing structures not yet fully understood and mimicked on traditional aircraft. Using a combination of their primary, secondary, and ulua feathers, birds can optimize their wing camber and twist distribution for all flight conditions whereas traditional aircraft via slats, flaps, and other wing mechanisms are able to optimize for a handful of conditions including landing, takeoff, and cruise [Dvorak(2016)]. Birds also utilize the bell-shaped lift distribution (discussed more in section 1 1.3.3) rather than the widely known elliptical lift distribution which not only lowers the induced drag, but also allows for the removal of the vertical stabilizer due to proverse yaw achieved in the outer portion of the wing[Bowers and Murillo(2016)].

Sea birds are the primary subject for biomimicry in this thesis. They have "requirements" similar to man-made aircraft: they fly faster, soar for longer periods, expect relatively consistent winds, and do not need to maneuver a great deal [Dvorak(2016)]. Particularly, the albatross is the primary subject for comparison.

1.3.2 Morphing Geometry

The first morphing geometry used in an aircraft was the wing warping on the Wright Flyer. Although this use was for primary flight controls, morphing geometry in literature generally refers to changes made to improve performance over the flight envelope. Morphing geometry includes planform alteration (span, sweep, and chord), out-of-plane transformation (twist, dihedral/gull, and span-wise bending), and airfoil adjustment (camber and thickness)[Silvestro Barbarino(2011)]. Basic wing morphing includes flaps, slats, and other mechanisms, and only since the 1970s more advanced morphing techniques have seen wider use. Notably, the variable wing sweep has appeared on several aircraft including the F-14 and B-1 [Silvestro Barbarino(2011)]. Extensive research efforts have been devoted to variable sweep devices, but very little work has been done on variable twist geometry [Silvestro Barbarino(2011)] despite the possibilities for significant efficiency gains [Gilbert(1981)]. Nearly 40 years have past since the performance benefits of the Mission Adaptive Wing System (MAW) (a wing camber mechanism applied to F-111) were first described in detail [Gilbert(1981)], and yet the wing twist technology has yet to leave the realm of X-planes and UAVs [Silvestro Barbarino(2011)]. After MAW, additional incremental improvements have been made to the variable twist design for decreasing weight and allowing

for significantly more twist and variation of the twist distribution
[Marks et al.(2015)Marks, Zientarski, Culler, Hagen, Smyers, and Joo].

Birds vary their span during dives and other maneuvers, and constantly vary their twist angle to achieve peak performance [Dvorak(2016)]. This study attempts to partially mimic a bird's variable wing twist utilizing a full moving outer wing section (outeron) to increase aircraft efficiency. Varying the outeron's angle will allow the aircraft to stay closer to the desired bell-shaped spanload over a wide range of flight conditions.

1.3.3 Optimal Spanloads

Aerodynamic efficiency drives key aircraft performance metrics such as range, payload, and endurance. Many studies have been devoted to most efficient way to distribute lift along the wing, called the optimal lift distribution, or alternatively, the optimal spanload.

Prandtl, in 1922, proposed lift and span as constraints, leading to the elliptical lift distribution as the optimal solution for minimizing the induced drag. The lift distribution on an elliptic wing of span 'b' is given by

$$L' = L'_0 \left(1 - \left(\frac{y}{b/2}\right)^2\right)^{1/2} \tag{1.1}$$

However, if the span constraint is removed and the root-bending-moment is kept constant, then the bell-shaped-spanload is optimal for minimizing the induced drag. This was identified by Prandtl in 1933[Prandtl(1933)], as well as later by R.T.Jones at NACA [R.T.Jones(1950)].

$$L' = L'_0 \left(1 - \left(\frac{y}{b/2}\right)^2\right)^{3/2} \tag{1.2}$$

Both spanloads given by eq 1.1 and eq 1.2 are shown in Fig. 1.1, scaled to produce the same lift and same root-bending moment, yet the bell-shaped lift distribution is 11% more efficient in terms of total induced drag [Bowers and Murillo(2016)].

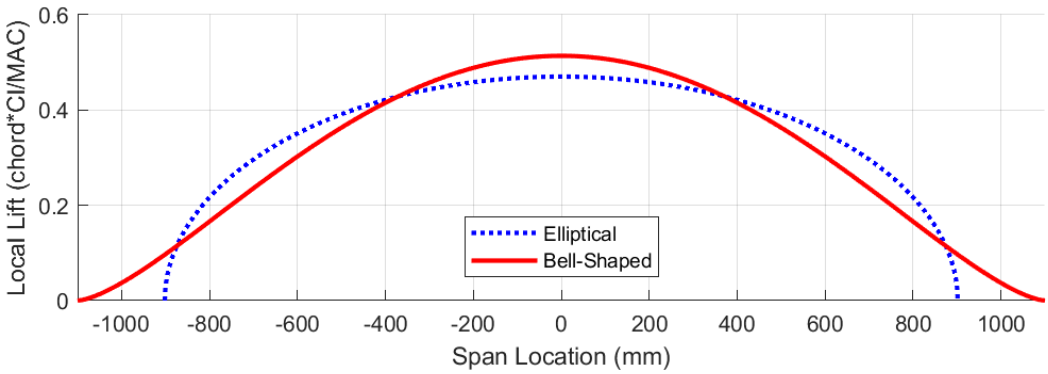

Figure 1.1: Comparison of Elliptic and Bell-Shaped Spanloads

Taking into account the viscous drag or higher fidelity parametric estimates for wing weight will result in optimal spanloads which generally lie somewhere between the elliptical and bell-shaped spanloads, as shown by Klein and others[Klein and Viswanathan(1975)][Wroblewski(2016)] [Iglesias and Mason(2001)][Munk(1923)][Cohen(1945)]. There are as many "optimal" spanloads as there are ways to constrain wing geometry but the goal of optimization has consistently targeted performance, namely reducing drag.

Unrelated to the search for high-aerodynamic-performance, the bell-shaped-spanload has implications for aerodynamic control.The bell-shaped-spanload has the novel property of trailing vortices shedding at a point mid-span rather than the traditional "wing-tip" vortices. This mid-span point is at approximately 70% of the half-span and occurs at the inflection point in the lift distribution[Bowers and Murillo(2016)]. In the region outboard of the mid-span vortex, partial induced-drag recovery is achieved in the form of "induced-thrust". The induced angle in this region tilts the Lift Vector forward which leads to induced thrust. This also has implications for proverse yaw; that is, the control deflections in this region cause positive yaw for positive roll [Bowers and Murillo(2016)].

Chapter 2

The Straight Flying-Wing

2.1 Motivation

Existing configurations of flying-wing bell-shaped-spanloads have been swept-back and include some dihedral. The Prandtl-D glider is a recent flying wing bell-shaped-spanload that will be used for comparison; the Prandtl-D uses 20 degrees of sweep [Bowers and Murillo(2016)]. Figure 2.1 shows a render of the Prandtl D glider model.

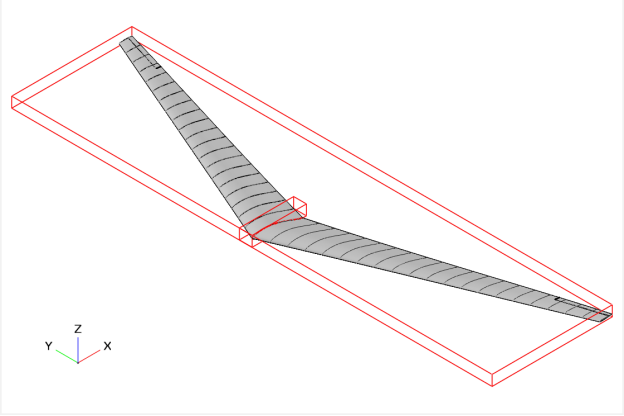

Figure 2.1: Prandtl D glider model

Straightening the wing offers certain advantages including a performance increase. If the bell-shaped-spanload gives the minimum induced drag (under certain constraints), then using it in the context of a swept-wing for non-transonic applications counteracts the benefit that is to be gained from the bell-shaped-spanload. To a first order approximation, efficiency

is proportional to $cos(\Lambda)$, implying that a 20-degree sweep results in roughly a 6% hit to aerodynamic efficiency, dihedral has a similar effect, though angles are typically small.

The impact to equilibrium and control is more subtle. Whether for different payloads or flying conditions, a versatile platform is expected to operate effectively at different overall lift coefficients. For a swept wing, these are achieved by shifting the trim angle of attack using elevon deflections. Thus, not only does the bell-shaped-spanload degrade in this configuration when operating at the non-design-point CL (with no way to correct it without adversely affecting trim), the elevon deflections necessary to fight static stability further degrade the lift-distribution. Particularly, this occurs at the wing-tips which are the critical locations for drag-recovery.

However, on a straight wing, control surface deflections have manageable pitching moments. Particularly, in a linear sense, variable quarter-chord twist at any span location has no pitching moment. This allows a variable twist device to optimize the lift distribution at each flight condition. As a result, the straight flying-wing is a suitable configuration for morphing structure applications. A morphing geometry with compliant structure is outside the scope of this study although a simple version of variable geometry is implemented to demonstrate the fundamental idea, the aforementioned outeron is a full-moving control surface which rotates about the quarter chord, which is effectively variable twist inserted at a discrete point. This all-moving outer surface also maximizes the bell-shaped-spanload proverse yaw effect (See Section 4, part 4.3) [Kuhlman(2003)].

2.2 Biom Configuration Features

The "Biom" (short for bio-mimicry) configuration is a straight flying-wing (zero quarter-chord sweep and zero dihedral) that uses a bell-shaped lift distribution. Recall that for bell-shaped lift distributions, the main wing vortex is not at the wingtip but rather at approximately 70% of the half-span; this location where the main wing vortex appears will be referred to as the vortex shedding line. The biom configuration has two sets of control surfaces used for lateral-directional control: one placed inboard of the vortex shedding line (innerons), and one placed outboard of the vortex shedding line (outerons). Figure 2.2 shows a sketch of the biom configuration.

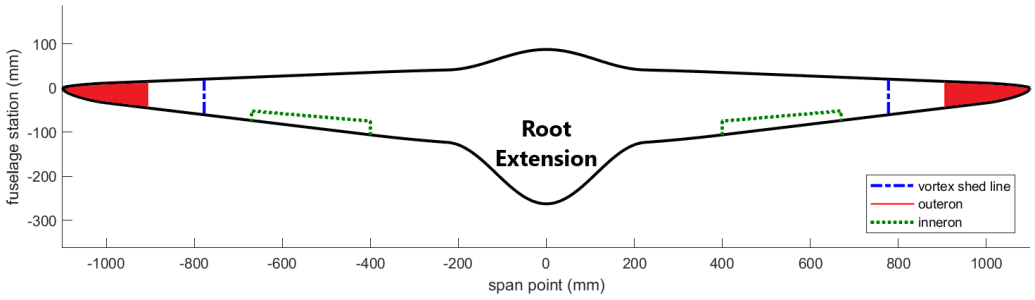

Figure 2.2: Biom configuration overview

This particular arrangement of control surfaces makes the lateral-directional system fully controllable and thus fully stabilizable (see section 2.3.2).

The biom configuration also includes a root-extension and/or a root-body elevator to improve longitudinal control.

2.3 Design Risks

2.3.1 Longitudinal Dynamics

Longitudinally, the straight-flying-wing is an undesirable conglomeration of poor flight dynamics characteristics; issues include:

- very low aerodynamic pitch damping
- very low pitch inertia
- small pitch moment arm - low control power
- airfoil pitching moments cannot be effectively trimmed - reflex is necessary
- only very small static margins are trimmable, static stability is very low at best

Despite these poor longitudinal characteristics, this general shape is found in birds (see Fig. 3.5). There are no apparent aerodynamic changes that would alleviate these issues short of abandoning the configuration altogether by adding back an empennage; these issues must be addressed head-on using high-gain closed-loop feedback control. Thus a discrete flight controller will take the role of a bird's "balance" or "piloting".

Collective inneron deflections could be used for pitch control, however a root-body elevator is used for more control power. The root-body elevator in this case is analogous to a bird's tail.

Note that birds may use small changes in sweep for pitch control, directly manipulating the center of lift and thus the pitching moment. However, the effectiveness of this method is proportional to the operating lift coefficient and thus cannot fully explain bird flight during all flight phases (e.g. in a dive). In any case, the manipulation of sweep for pitch control is not easily transferable to artificial flying vehicles due to the high demands on the sweep actuators (fighting a large moment of inertia) and the heavy hinges required (must carry all of the lift). Variable wing sweep as a primary flight control is outside the scope of this study, but again this shows that the configuration is suitable for further investigations into morphing geometry.

2.3.2 Lateral-Directional Control

With no sweep or dihedral, the vehicle will be spiral mode unstable. With no vertical surfaces and no sweep, sideslip dynamics will be unstable or insufficiently constrained. Active feedback control is thus necessary in both axes to stabilize the system. Given that a flight controller is necessary for longitudinal dynamics, this does not constitute a major configuration change. Sensors and control laws are addressed in section 4.4, aerodynamic control is further discussed in section 4.2.

Briefly, the idea behind the novel aerodynamic control scheme is as follows. Placing two sets of trailing edge control surfaces at different locations in the downwash distribution lead to two linearly independent control vectors in the lateral-directional control space.

The outerons are placed outboard of the vortex shedding line (see Fig. 2.2), in a region of upwash, and produce proverse yaw; that is, positive yawing moment for positive rolling moment.

A second set of control surfaces, the "innerons", are placed inboard of the vortex shedding line (see Fig. 2.2), in a region of downwash, and produces adverse yaw; that is, negative yawing moment for positive rolling moment.

These two control "directions" in roll and yaw imply that for any arbitrary desired roll and yaw command, there is some combination of differential inneron and outeron deflection that will result in that roll/yaw moment combination. In a linear sense, we expect a diamond-shaped control power region in the lateral-directional control space as shown in Figure 2.3

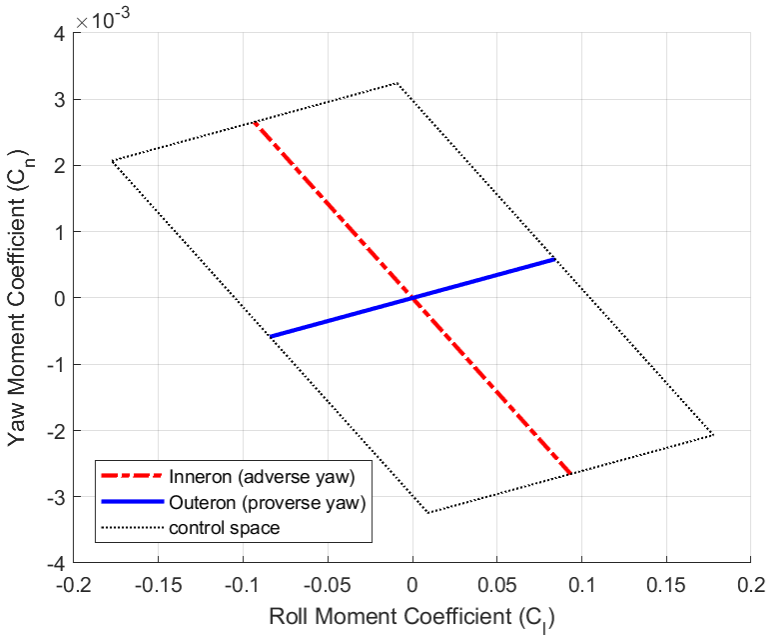

Figure 2.3: Lateral-Directional control space

The controllability of this configuration rests on having a proverse-yaw characteristic, which itself is only possible because of the induced angle distribution (upwash for wingtip and downwash elsewhere). The induced angle distribution comes from the bell-shaped-spanload, thus the viability of this configuration is dependent on the bell-shaped-spanload.

Chapter 3

Biom T1 - Vehicle Design

In order to study the viability of a straight-wing bell-shaped-spanload Biom configuration, the handling qualities of a 2.4kg, 2.2 meter wing-span UAV called "Biom T1" are examined. Figure 3.1 shows an isometric view of the Biom T1 CAD model. Table 3.1 provides the wing geometry definition.

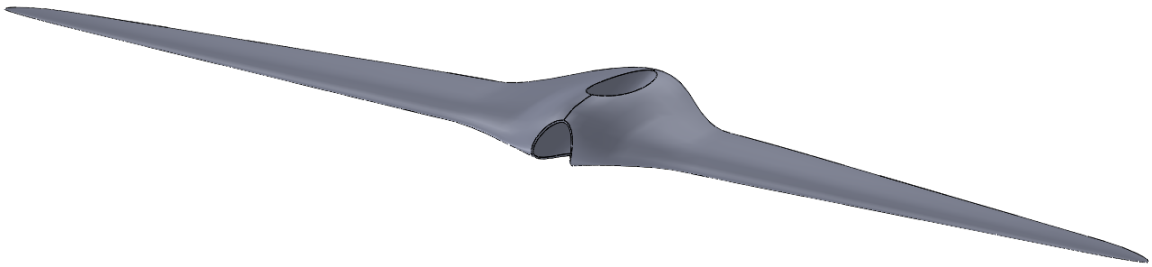

Figure 3.1: Isometric view of the Biom T1 CAD model

Table 3.1: Wing geometry definition

y(mm)	chord (mm)	twist(deg)	camber(%)	thickness (%)
0	350	2.9	3.0	24.6
20	346.5	2.9	3.0	23.7
45	332.8	2.9	3.0	20.1
75	305.0	2.9	3.0	14.2
100	275.5	2.9	2.5	10.4
125	243.9	3.4	2.5	10
155	208.4	4.1	2.5	10
180	184.7	4.6	2.5	10
205	169.4	5.2	2.0	10
225	164.1	5.1	2.0	10
315	153.9	5.05	2.0	10
400	141.5	4.95	2.0	10
600	109.3	4.65	1.0	10
750	85.2	3.6	1.0	10
906	60.2	2.2	0.0	10
1025	39.7	0.15	0.0	10
1080	19.3	-0.7	0.0	10
1090	13.3	-0.75	0.0	10
1100	1.0	-0.8	0.0	10

EH series tailless airfoils, designed by John Yost, are chosen for their wide range of camber and thickness; although, the exact thickness profile still necessitated modifications to thickness.

This geometry was developed by iterating on an initial bell-shaped planform shown in Figure 3.2.

Initial studies on the planform of Figure 6 indicated that this shape would produce a lift distribution very close to the ideal bell-shape defined by Eq. (1.2). The biggest issue with this shape is the wingtip, which steeply narrows to a point. This is not particularly manufacturable, does not match the planform shape observed in birds, and critically does not have good lateral-directional control (not enough area for control surface at wingtip, see section 4 4.2 4.3). The planform requires additional area at the wingtip and washout to correct the lift distribution back to bell-shaped-spanload. This is a beneficial relationship

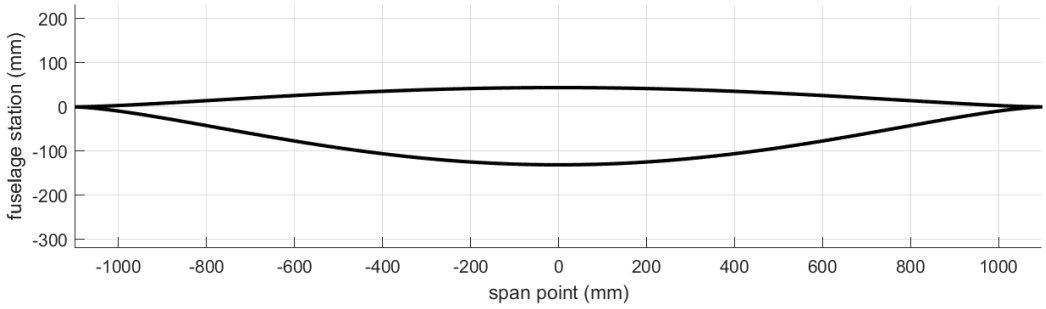

Figure 3.2: Initial Bell-Planform

since it also tends toward the wingtip stalling later than other parts of the wing, maintaining control during a partial stall.

3.1 Geometry Determination

The Biom T1 chord as a function of span is defined in four sections. All sections build upon an underlying bell-planform: this defines the chord as a function of span according to Eq. (1.2) used for the bell-shaped-spanload. Going from inboard to outboard, the four sections are:

- Cosine Root Extension
- Pure Bell Region
- Linear Taper Region
- Elliptical Taper Region

Figure 3.3 shows the four planform sections.

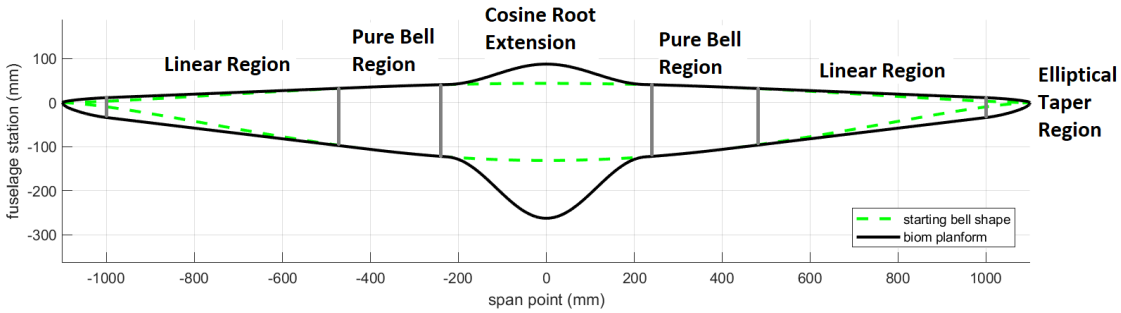

Figure 3.3: Biom planform sections

3.1.1 Cosine Root Extension

Having a larger root chord has many advantages in the Biom configuration. Larger chord results in a greater moment arm for the elevators, which are two plain flaps located around the root chord. Also, a larger chord results in a greater total thickness for a certain airfoil percent-thickness. Large total thickness at the root is useful for storing fuel, avionics, and general payload. In order to maintain the bell spanload at cruise, the root section must be twisted to a lower angle resulting in a lower local lift coefficient. This yields the same benefit as seen in the wingtip: this portion of the wing will stall later, allowing good pitch control to be maintained through a partial stall.

To have a smooth transition into the root extension from the pure bell-region, a cosine function was used to define the shape of the root extension, which is superimposed onto the bell-shaped planform. Thus this region is not fully defined by either a cosine function or bell function alone.

3.1.2 Pure Bell Region

This portion of the wing is purely unmodified bell-planform and is the region which will stall first. There are no aerodynamic controls in this region.

3.1.3 Linear Taper Region

To increase the chord around the wingtip, a "target" tip chord is selected and the entire outer portion of the wing is straight tapered to meet this tip chord condition. To determine where the linear region begins, a tangency constraint is applied against the unmodified bell-planform.

3.1.4 Elliptical Taper Region

Since the outer portion of the wing is intended to move as a flight control element and is scheduled for performance, there should be no sharp discontinuity right at the wingtip. This improves the ability for the single-degree-of-freedom outeron schedule to actually match the bell-shaped-spanload more closely at different flight conditions.

A fader multiplier that goes from 1 to 0 is applied in this region; the equation for an ellipse is used. Again, since this is a multiplier applied to the linear taper region, this region is not fully defined by the equation for an ellipse. Figure 3.4 shows the geometry buildup for the Biom T1.

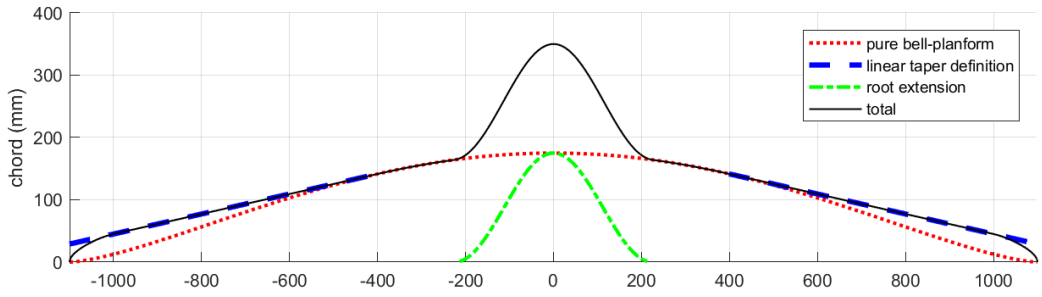

Figure 3.4: Geometry Buildup for Biom T1

3.2 Comparison to Albatross

This geometry parameterization, while developed for the Biom T1 design, can define an entire family of Biom aircraft, and can even be used to approximate the geometry of an albatross. The biggest differences being that the albatross appears to generally fly with swept wingtips (exaggerated in Fig. 3.5 below), and the head extends further forward than parameterized. Table 3.2 shows the comparison of geometry parameters of the biom-approximated albatross and Biom T1.

Table 3.2: Comparison of geometry parameters of albatross and Biom T1

parameters (mm)	Albatross	Biom T1
bell root chord	250	175
half span	1500	1100
cosine span	150	225
cosine chord	400	175
linear tip target	40	29
ellipse width	150	100

Figure 3.5: Overlay of Biom-Para

3.3 Thickness Profile

A limitation of the Biom configuration is the internal volume. For tradespace studies using the Biom T1 geometry, a turbojet was selected for the design power system since it is of high power density with high energy density fuel (as opposed to batteries). For future flight test studies with this configuration, an electric ducted fan may be used in place of a small turbojet or turbofan; this has lower cost and worse performance, but is acceptable for aerodynamic characterization during flight test.

In any case, the thickness profile is designed around internally fitting a 70mm diameter airpath that goes all the way through the vehicle axially. The presence of such an air path for a turbojet or ducted fan is directionally destabilizing, but a statically stable airframe is not a necessary prerequisite for Biom based design. Nonetheless, this must be modeled and

accounted for during control law design and for T1 this was part of the robustness analysis (see Table 4.4).

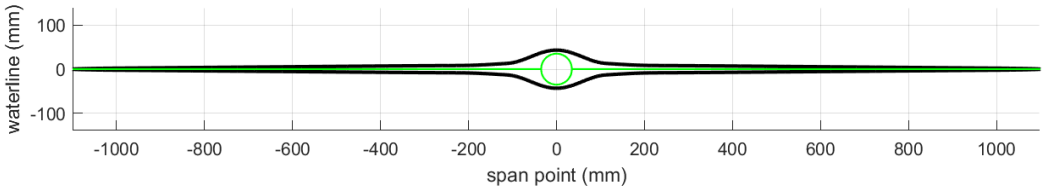

Figure 3.6: Thickness profile, front view

A constant 10% thickness is applied everywhere, causing the absolute thickness to bear a similar shape to the planform itself. However, additional thickness is required at the root to allow the airpath, so a cosine function is again superimposed to meet the root thickness requirement. The flow in this maximum thickness region is somewhat separated, and as a result, the elevators are placed on either side of this region but do not extend into it. This simplifies longitudinal control law design since the elevators are not in the high energy flow downstream of the power system. If they were, control power would vary with throttle setting causing a troubling non-linearity. It would also necessitate the implementation of hinge-moment restriction tables to prevent overloading the actuators driving large deflections into high energy flow. Figure 3.6 shows the front view of thickness profile, Fig. 3.7 shows the % thickness distribution along the span, and Fig. 3.8 shows the thickness distribution of various components along the span.

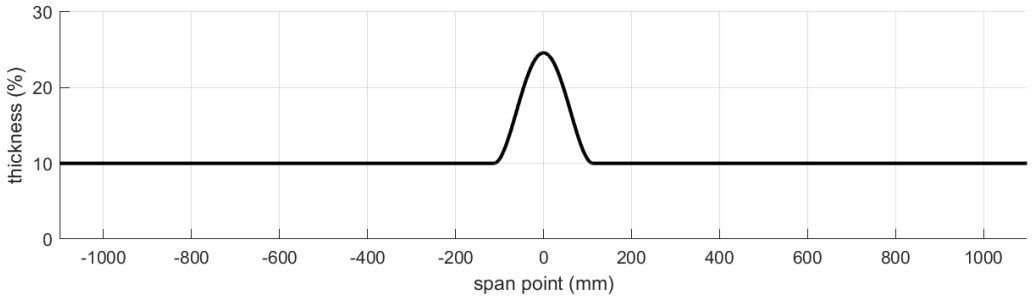

Figure 3.7: Percentage thickness distribution along the span

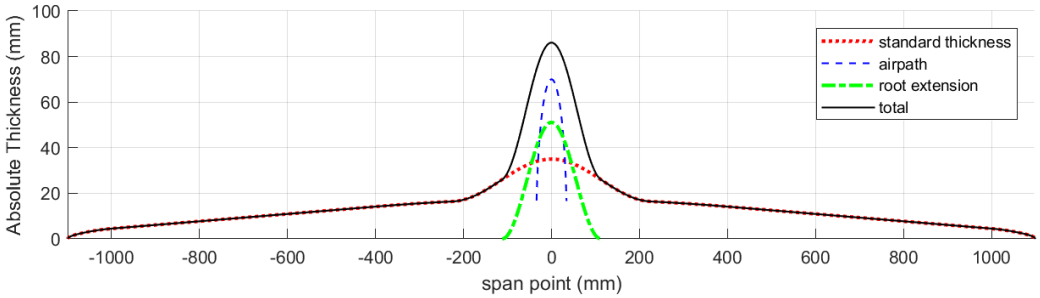

Figure 3.8: Thickness distribution along the span due to various components

3.4 Aerodynamic Characteristics Over Span

To get the bell-shaped lift distribution, a simple inverse method was applied wherein the geometry was determined by the desired flow instead of the flow analyzed for a given geometry. A linear "Twist Predictor" was used to estimate the initial twist that was necessary in order to get a bell-shaped-spanload in the presence of the (assumed) induced angle distribution that would be caused by a bell spanload. The target lift distribution, Biom T1 chord distribution, and the flight condition design point are all used to calculate the target lift coefficient distribution. Figure 3.9 shows the assumed downwash and target lift coefficient along the span.

The twist prediction uses a linearized version of the airfoil to convert from target lift coefficient to target angle of attack (AOA). From target AOA and assumed downwash, the twist is predicted. The final twist distribution differed from the target primarily due to the linearization process.

Calculated lift distribution and other spanwise distributions are shown in Figures 3.11-3.15, calculated using the XFLR5 vortex latice method (VLM2). Cruise speed used in all analysis was 20 m/s.

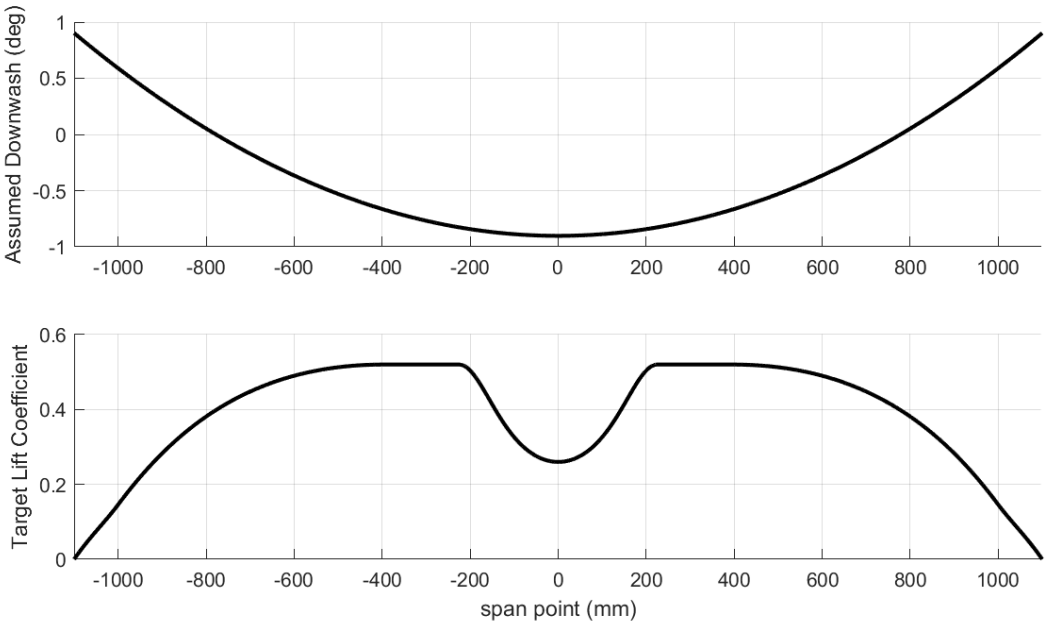

Figure 3.9: Assumed downwash and target Cl distribution along the span

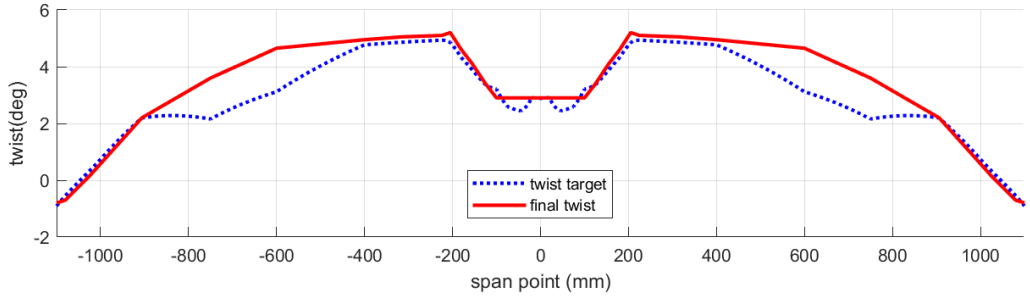

Figure 3.10: Twist prediction

This design shows both induced thrust on the outboard portion of the wing as well as low total induced drag. Since this was an inviscid panel method analysis, the "Local Drag" plot only differs from the "induced drag coefficient" plot by the chord weighting as a function of span.

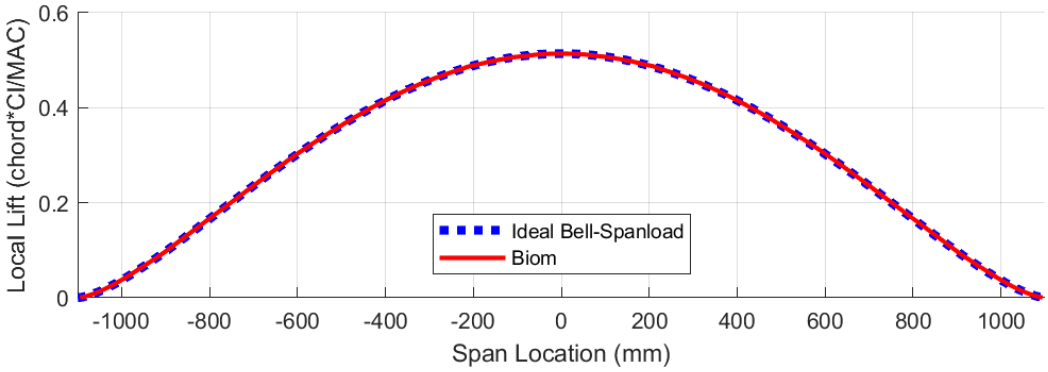

Figure 3.11: Calculated lift distribution comparison against the ideal lift distribution

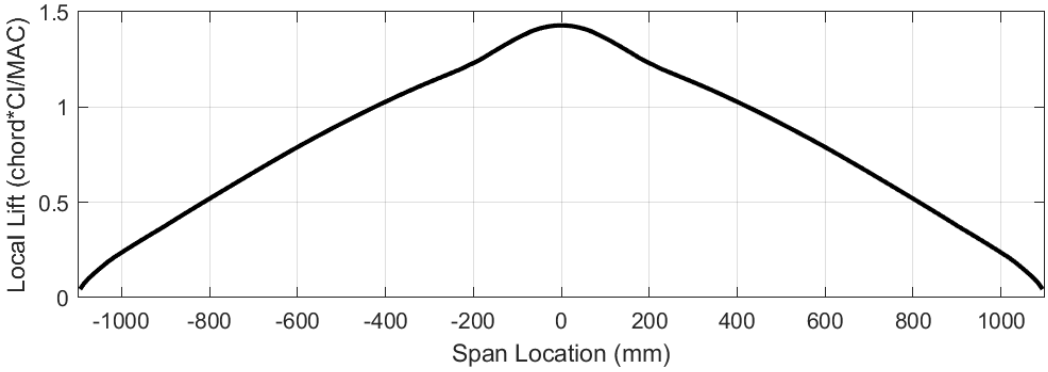

Figure 3.12: Lift distribution near stall

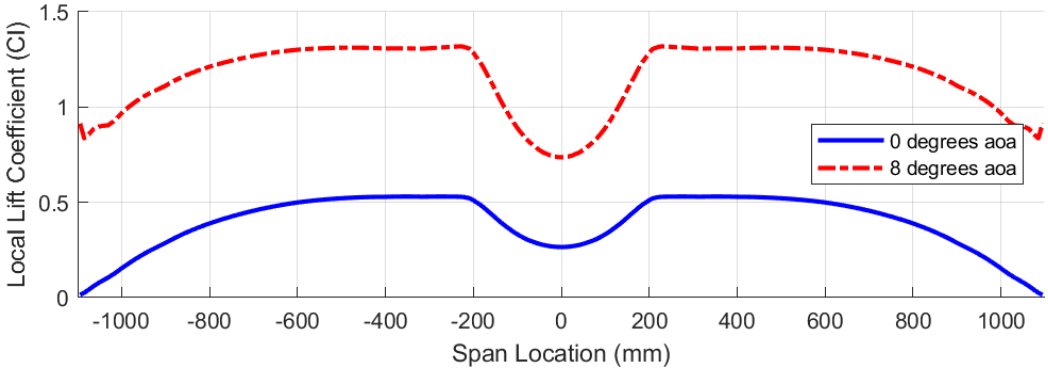

Figure 3.13: Lift coefficient distribution at cruise and near stall

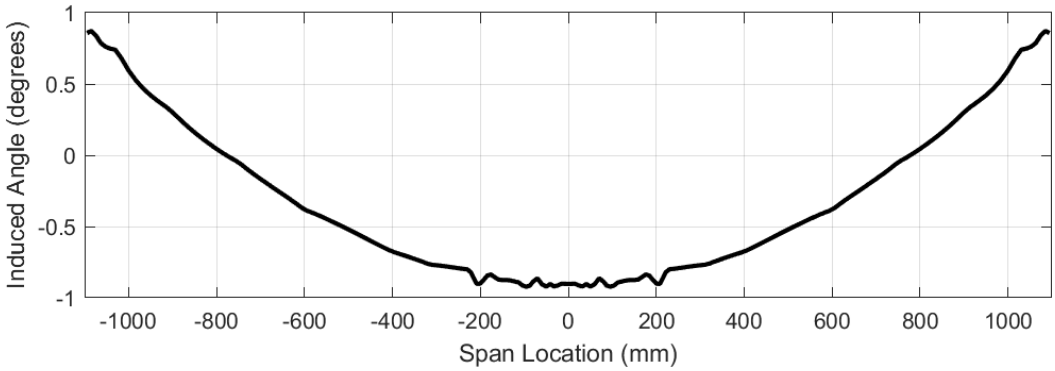

Figure 3.14: Induced angle distribution at cruise

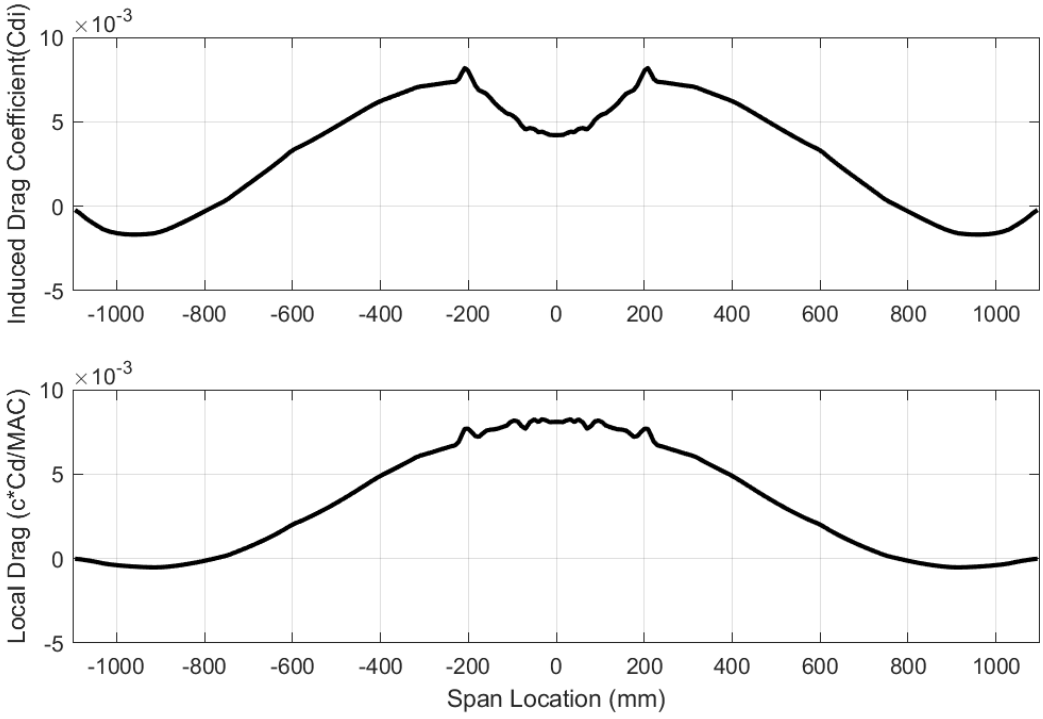

Figure 3.15: Induced and local drag distribution at cruise

Chapter 4

Biom T1 - Stability and Control Analysis

4.1 Stability - Linear Plant Characteristics

Longitudinally, both modes are poorly damped as expected. However, the ratio of control power to stability is high (approaching infinity for the neutrally stable pole-pair near the origin) meaning the longitudinal plant characteristics allow for closed-loop stabilization. Figure 4.1 shows the longitudinal open-loop eigenvalues.

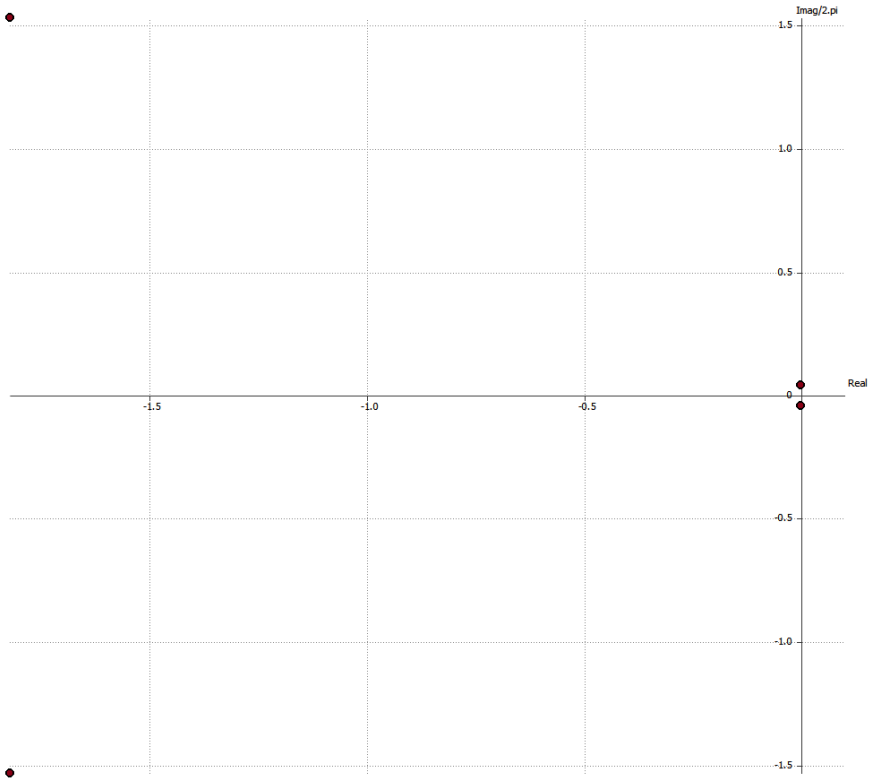

Figure 4.1: Longitudinal Open-Loop Eigenvalues

Lateral Directional eigenvalues look comparatively better: The spiral mode time to double is high, the low aerodynamic response in yaw has nearly eliminated the dutch roll response (making it easy to actively control), and roll subsidence is great. Figure 4.2 shows the lateral-directional open-loop eigenvalues.

One issue with designing a flight controller for this plant is that with such low sideforce generated or any aerodynamic moments with respect to sideslip, an observer will have trouble estimating the sideslip; direct measurement of sideslip may be necessary and for flight test development creating an observer that would work for this aircraft is considered high risk. In our study, we settled on a simple 2-hole probe which only measures sideslip (see section 5 5.1).

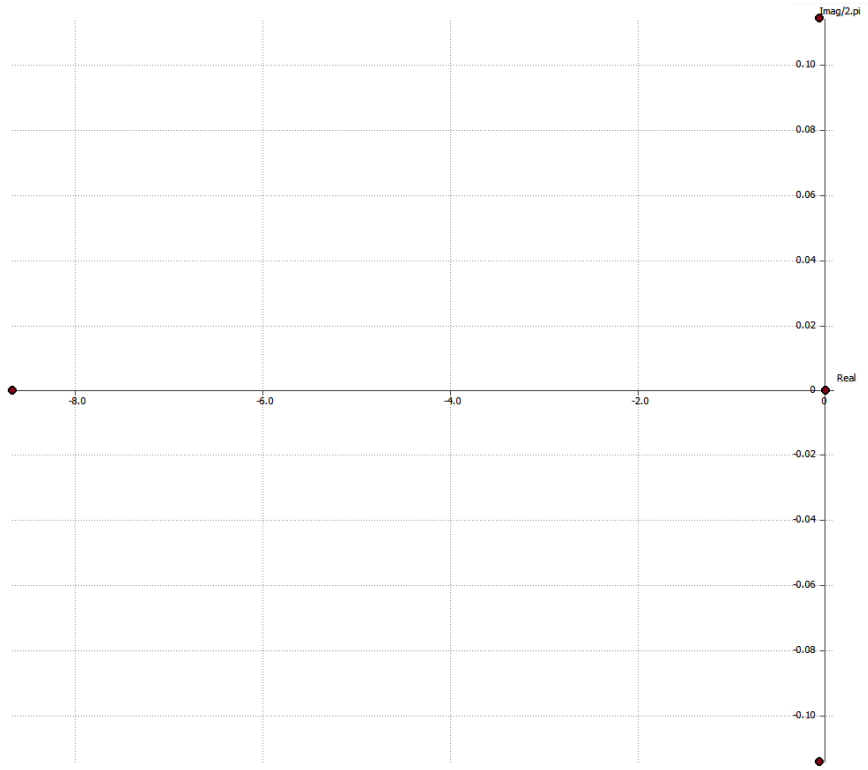

Figure 4.2: Lateral-Directional Open-Loop Eigenvalues

4.2 Control

XFLR5 is useful for quick design iterations in developing the geometry but lacks key capabilities for analyzing the effect of control surfaces. Namely, the induced drag distribution caused by asymmetric control deflections cannot be accessed or exported; only the total moments are outputs of the computer program for asymmetric wings. As a result, Biom T1 was also modeled in OpenVSP, another vortex-lattice software which has more options for control surface configuration and analysis. One drawback with this analysis is that the left and right wings are not properly merged resulting in some lost lift near the root. The solver also exhibits numerical dispersion in induced drag, but this appears to settle before the wingtip, where one cares most about the induced drag changes. Both drawbacks are not suitable for performance analysis, but should not appreciably impact control analysis which depends on changes far from these regions of distortion. Root sections should be ignored in spanwise plots. Figure 22 shows Biom T1 with control surfaces defined in OpenVSP.

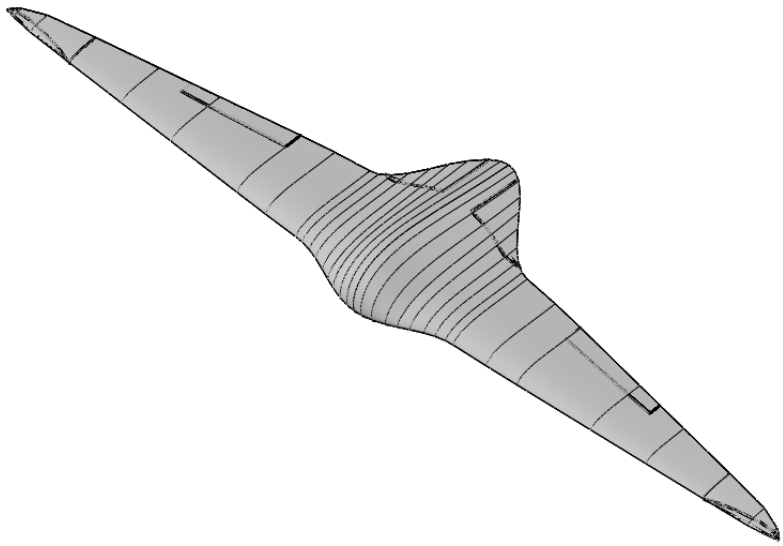

Figure 4.3: Biom T1 with control surfaces defined in OpenVSP

4.2.1 Elevators

The elevator chord fraction starts at 0.29 at the 70mm span point and tapers to zero at the 216mm span point. The elevator is split up to accommodate the trailing-edge curvature, provide redundancy, and simplify control analysis. Neutral stability is targeted, so that cruise at all flight conditions is achievable with no steady state deflections, only small corrective transients. Table 4.1 gives the longitudinal control derivatives.

Table 4.1: Longitudinal Control Derivatives

	$X_{\delta e}$	$Z_{\delta e}$	$M_{\delta e}$
Elevator	-0.18	-7.0	-1.4

4.2.2 Innerons and Outerons

Control power was determined from small (2 degree) deflections for a finite difference approximation of linear control power near the neutral position. The innerons start at $\frac{y}{b/2} = 0.36$ and end at $\frac{y}{b/2} = 0.61$ using a chord fraction of 0.22. The outerons start at $\frac{y}{b/2} = 0.82$ and are all-moving. Figures 4.4 and 4.5 show the lift and drag distributions respectively along the span in openVSP with different control deflections.

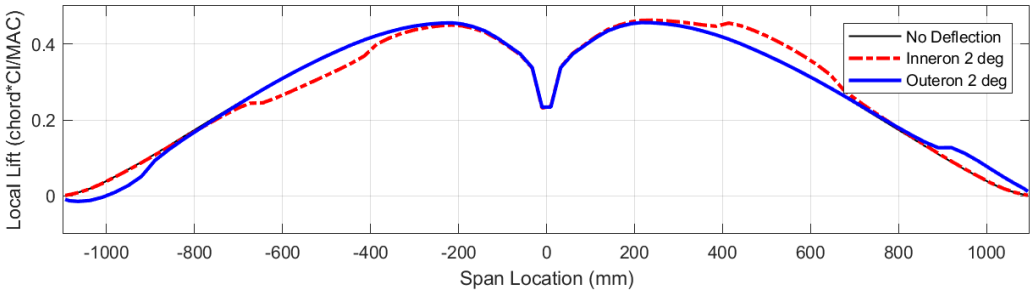

Figure 4.4: Lift distribution in OpenVSP with different control deflections

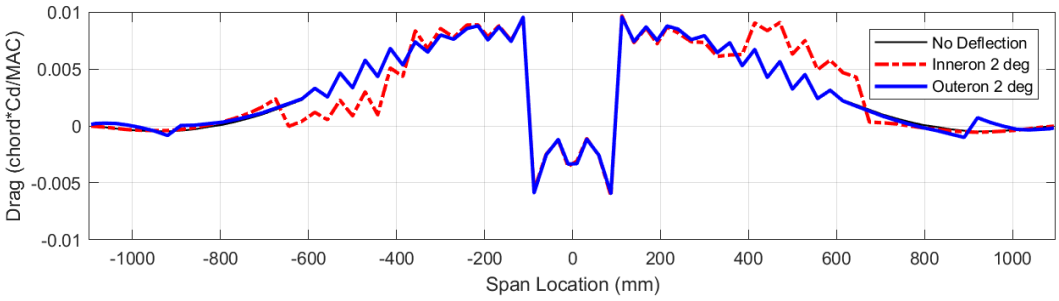

Figure 4.5: Drag distribution in OpenVSP with different control deflections

The lateral-directional control derivatives are given in Table 4.2 in units of rad^{-1}.

Table 4.2: Lateral-directional control derivatives

Surface	$C_l\delta a$	$C_n\delta a$
Inneron	-0.5354	0.0152
Outeron	-0.4828	-0.0034

Biom T1 does achieve proverse yaw using the outerons (see Fig. 2.3), but not entirely in the manner expected. Focusing on the effect of the outeron on the outboard wing, Figs. 4.6 and 4.7 show the drag on left and right wing respectively due to 2 degree outeron deflection.

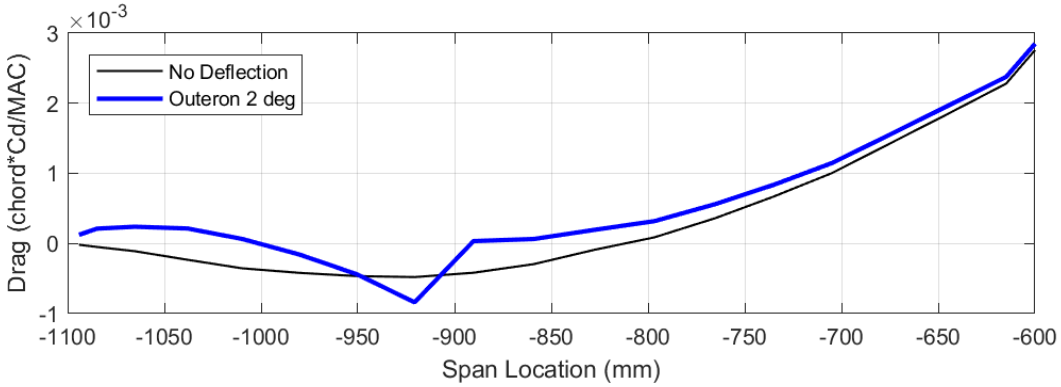

Figure 4.6: Left wing drag with and without outeron deflection

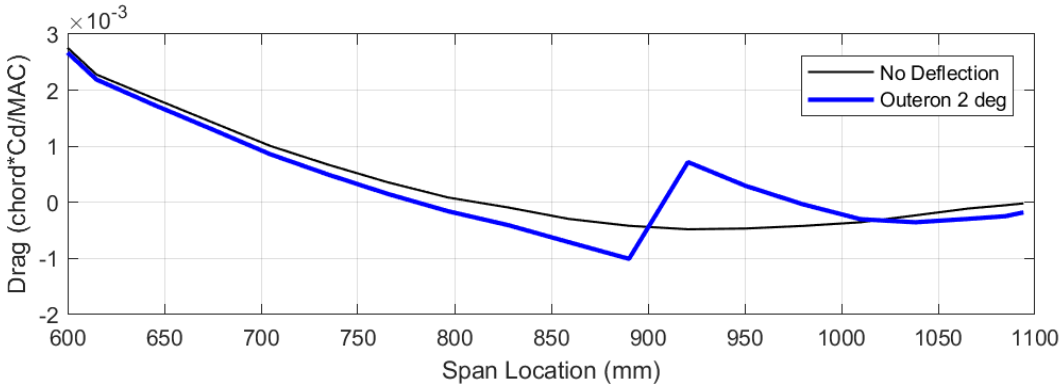

Figure 4.7: Right wing drag with and without outeron deflection

The outeron starts at span location 906 mm and the change in lift in this region changes the flow inboard of the outeron. From span location 600 mm to 906 mm, there is a change in induced drag that has a proverse characteristic; the right wing is producing additional lift (left roll), and more negative induced drag (left yaw). The region of the outeron itself however has no well defined characteristic; on the right wing it is mostly adverse, and on the left wing it is mostly proverse.

Evaluating the area "under the curve" between no deflection and two degrees outeron deflection, it can be seen that the left wing is a greater contributor to the total yawing moment,

and there is still overall more drag when the controls are deflected. On the right wing (advancing in yaw), the total drag difference is positive albeit barely.

If, on the other hand, the advancing side was found to be actively pulling that wingtip forward through additional induced thrust, it would raise doubts on why the outerons are not permanently left in a symmetrically deflected condition that produces additional induced thrust. Thus, it should not be surprising that the mechanism for proverse yaw is through net drag.

Control analysis of the Prandtl-D glider showed nearly identical behavior for a differential elevon deflection, giving more explanatory scope to this model of how proverse yaw is produced on bell spanload wings. Even with no net yaw moment caused by the "lifting-side," this is still an improvement over what would otherwise be a strong adverse yaw response for the same rolling moment. Additionally, given some portions of increased induced thrust that are being canceled out by increased drag elsewhere, the net drag for a given roll moment is less than that of a conventional aileron control scheme.

Regions of induced thrust result in a much reduced drag increment per yaw moment increment. Sectional induced thrust ($T'_{induced}$) is the component of sectional lift aligned with the body-x axis:

$$T'_{induced} = L' \cdot \alpha_L \tag{4.1}$$

Since $\alpha_L = -\frac{\omega_L}{V_\infty}$,

$$T'_{induced} = -L' \cdot \frac{\omega_L}{V_\infty} \tag{4.2}$$

where L' is sectional lift, α_L is local angle of attack, ω_L is the local downwash, and V_∞ is the freestream velocity (note that small angle approximations were used for α_L). Differentiating with outeron deflection (positive is right trailing edge down), δ_{out} yields an expression for the control contributions to induced drag for a particular airfoil section as:

$$\frac{\partial T_{induced}}{\partial\ \delta_{out}} = \frac{1}{V_\infty}\left[\frac{-\partial L}{\partial \delta_{out}} \cdot \omega + L \cdot \frac{-\partial \omega}{\partial \delta_{out}}\right] \tag{4.3}$$

First consider the region of the outeron itself: the $\frac{-\partial L}{\partial \delta_{out}} \cdot \omega$ term is positive (this region is in upwash, thus ω is negative), which drives more induced thrust; however the $L \cdot \frac{-\partial \omega}{\partial \delta_{out}}$ term is negative. Given the decrease in induced thrust seen in Fig. 4.7, the latter term is dominant in this region.

In the region inboard of the outeron, the lift isn't changing much so the $\frac{-\partial L}{\partial \delta_{out}} \cdot \omega$ term is near zero, but the downwash is more negative as a result of the lift generated by the outeron, so the $L \cdot \frac{-\partial \omega}{\partial \delta_{out}}$ term is positive, resulting in an increase in induced thrust in this region (Fig. 4.7).

If the outeron covers too much span, there is less of a region of induced drag recovery inboard of the outeron. If the outeron covers too little span, the lift generation from the outeron doesn't produce a strong enough vortex to considerably influence the upwash distribution inboard of the outeron. The optimal span fraction for proverse yaw is expected to be at a local maximum somewhere in the middle; this motivated a span fraction study (see section 4.3 below).

The magnitude and perhaps the behavior itself is dependent on the wing loading. That is, higher design lift-coefficients have greater induced angles which create more robust induced thrust in the outer-span regions which create a favorable environment for proverse yaw even under large control deflections. In the limiting case (zero lift) it is apparent that the induced-angle distribution would be zero across the wing and thus proverse yaw cannot be achieved through these means. Higher wing-loadings are advantageous for dynamic soaring flight which is a potential application.

4.3 Optimizing Planform for Control Power

Before the Biom T1 design was developed, control power variations were tested on a "baseline" biom with squared-off wingtips instead of the T1 elliptical fade.

The main trapezoidal section of the "baseline" biom was changed in aspect ratio, taper ratio, twist distribution, and wing area in various ways to assess if there was any impact on the control power. Before the Biom planform was optimized, the baseline Biom had traditional

outer control surfaces as opposed to the full moving outeron seen on T1. After the first test with full-moving (FM) outerons, it was apparent that they greatly increased proverse yaw control power and therefore all subsequent designs included full-moving outerons. Varying the bell-shaped lift distribution (increasing twist at the wingtips) and increasing the span with no change in twist distribution led to large increases in proverse yaw control power. However, the planform changes had significant drawbacks. Varying the twist distribution increased the induced drag and enlarging the span increased skin friction drag. Ultimately, Biom T1 implemented the FM outerons since this increased proverse yaw control power without any performance losses during cruise. Figure 4.8 shows the yaw moment coefficient C_n vs. roll moment coefficient plot for various aircraft for 2° differential outeron deflection.

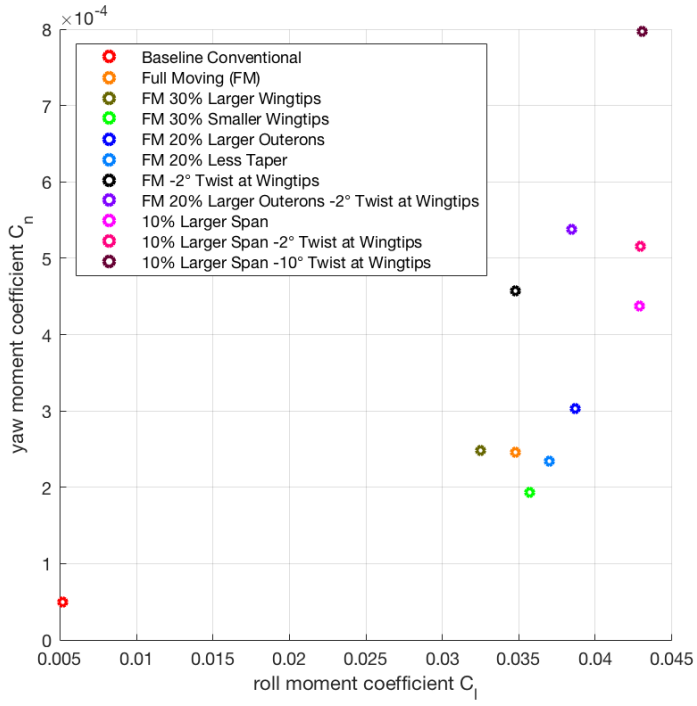

Figure 4.8: *Cn* vs *Cl* plot for 2° outeron deflection for various aircraft

After the general control power study, a spanwise fraction study on the placement of the outeron was conducted. The start location of the full moving outeron was varied from 71.2% of the span (just beyond the vortex shedding line) through 90.4%. A local maximum for

proverse yaw control power exists around 82.0% of the overall half-span. This matches the expectation for a local maximum identified in section 4.2.2.

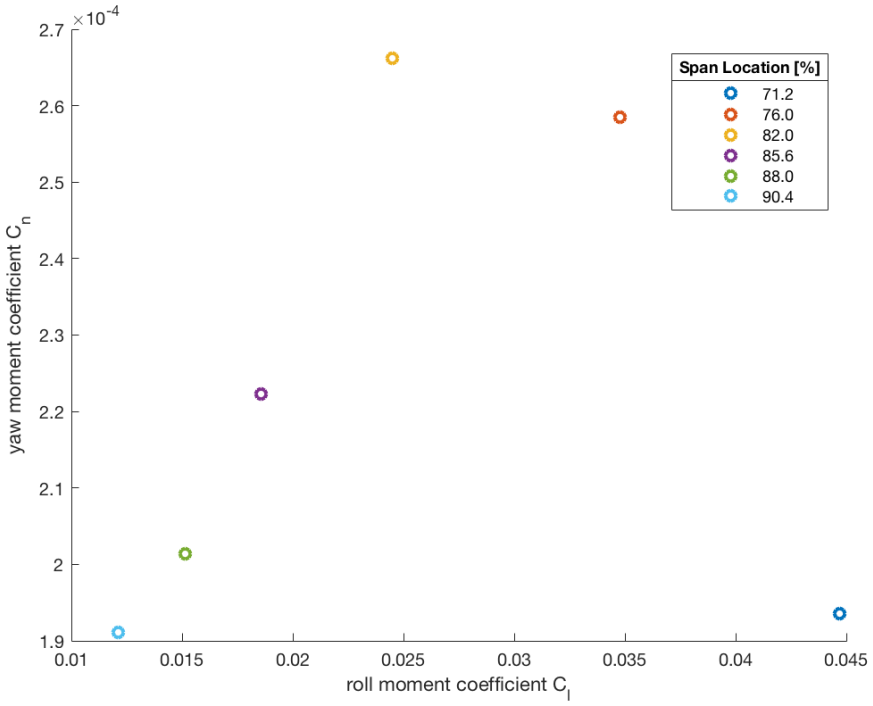

Figure 4.9: C_n vs. C_l with varying span fraction of the outeron at 2° deflection

As a result of the spanwise study, the outeron was placed at approximately 82% of the span fraction rather than at the start of the upwash region.

4.4 Closed-Loop Control

Biom T1 depends on a closed-loop flight controller to improve flying qualities. For this study, robust-servo linear-quadratic-regulator (RSLQR) was used for both longitudinal and lateral-directional control laws. Longitudinal Control tracks an Nz command, lateral control tracks p, and directional control tracks β.

In the lateral-directional plane, applying state-feedback to the augmented control matrix yields two virtual surface commands: differential inneron and differential outeron.

While real-time gains are scheduled to calibrated airspeed and angle of attack to create a non-linear control system, only linear analysis results are discussed here.

4.4.1 Longitudinal Control

For optimal feedback, only the integral-Nz state was penalized to generate gains K_{lqr}. The plant model for gain design does not include the actuator dynamics so that by comparing the stability robustness of the "closed loop" design against a "delta disturbance" formulation of the actuator dynamics, the required actuator bandwidth can be determined as:

$$\Delta_{act} = \frac{-s^2 - 2\zeta\omega s}{s^2 + 2\zeta\omega s + \omega^2} \tag{4.4}$$

If there is separation between the two curves, the system is robust to the disturbance. In this case, higher bandwidths push the actuator disturbance off to higher frequencies. At a bandwidth of 9Hz, the system is robust to the actuator, with margin. Figure 29 shows the robustness to actuator dynamics.

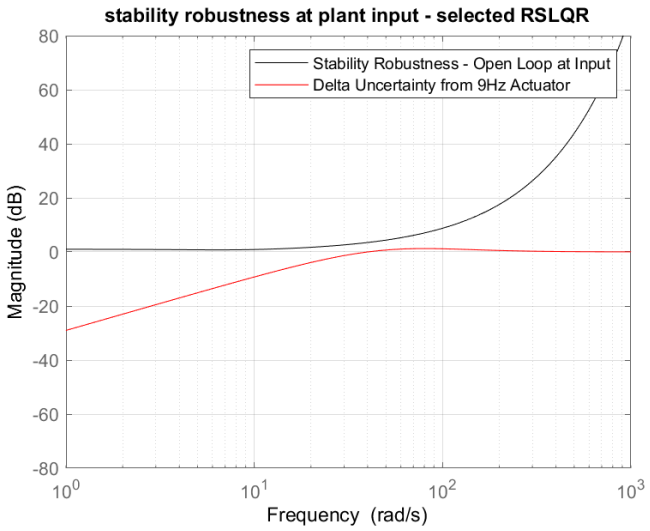

Figure 4.10: System robustness to actuator dynamics

One off the shelf servo that was characterized was the DS95i, which was designed for helicopter tail yaw control. The bandwidth of this actuator was estimated to be at least 13Hz, demonstrating 9Hz is a low-risk achievable target for small UAVs. Even cheap servos not geared for digital integration appeared to have a bandwidth of about 9Hz.

The selected gains resulted in the closed-loop step response shown in Fig. 4.11.

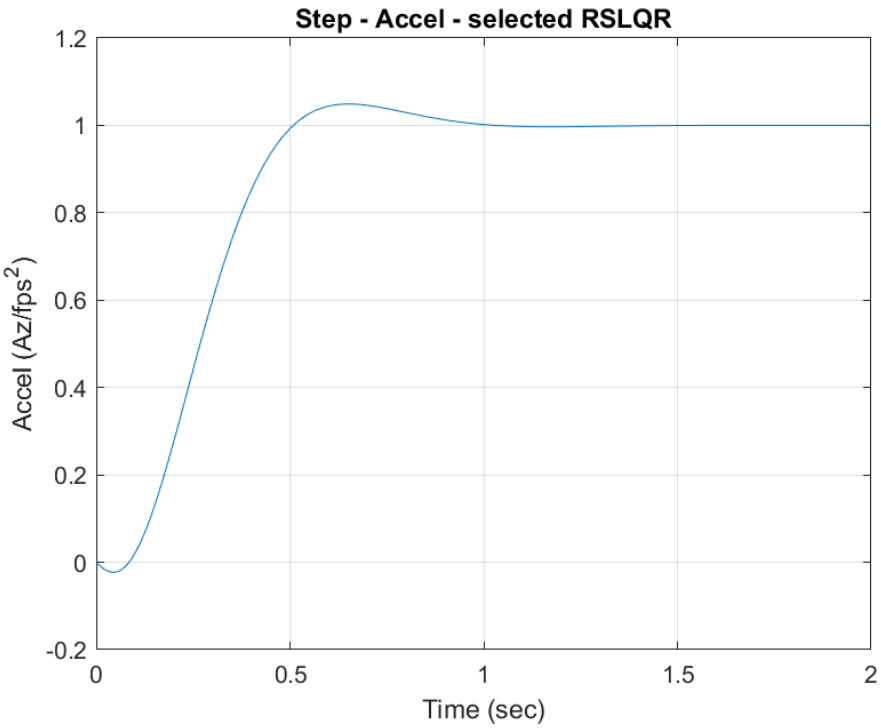

Figure 4.11: Acceleration timehistory step response

There is a overshoot but overall response is good; the system is non-minimum-phase due to the aft elevator placement, therefore there is some undershoot.

As a linear robustness study, this controller design was tested against variations in the plant model to generate the closed-loop dynamics and demonstrate robustness. Table C.1 shows the variations in longitudinal response and stability margins.

The gain and phase margins are worst case minimum singular value margins and thus are much less forgiving than classical margins. The baseline design is just about 5dB and 45deg phase, and in general does not degrade below 4.5dB and 40deg. Because the aerodynamic damping is so small, a wider range of uncertainties were used, demonstrating that even with zero damping the system is stable with poor but acceptable margins (3.1dB and 25.2degrees) given the extreme test condition. Figure 4.12 shows the variation in Nz time history of step response and the baseline system is represented using the dashed black line. Figure 4.13

Table 4.3: Longitudinal robustness variations

variation	rise time	settle time	GM	PM
BASELINE	1.97	2.00	4.9	44.8
Iyy -30%	1.77	1.79	5.2	48.5
Iyy +30%	1.71	1.99	4.6	40.3
Mde -30%	1.95	2.00	4.6	40.4
Mde +30%	1.94	2.00	5.1	47.5
Mq +100%	1.95	1.96	4.9	44.6
Mq = 0	1.81	2.00	3.1	25.2
Mw -50%	1.97	2.00	5.0	45.9
Mw +50%	1.98	2.00	4.8	43.8
Zde -50%	1.95	2.00	5.0	45.6
Zde +50%	2.00	2.00	4.9	44.0
Zw -50%	1.86	1.99	5.4	50.9
Zw +50%	1.92	1.93	4.5	39.3
m -20%	1.90	2.00	4.7	41.5
m +20%	1.97	1.98	5.1	47.0

shows the root locus as part of the robustness studies and the baseline system is represented using black X markers.

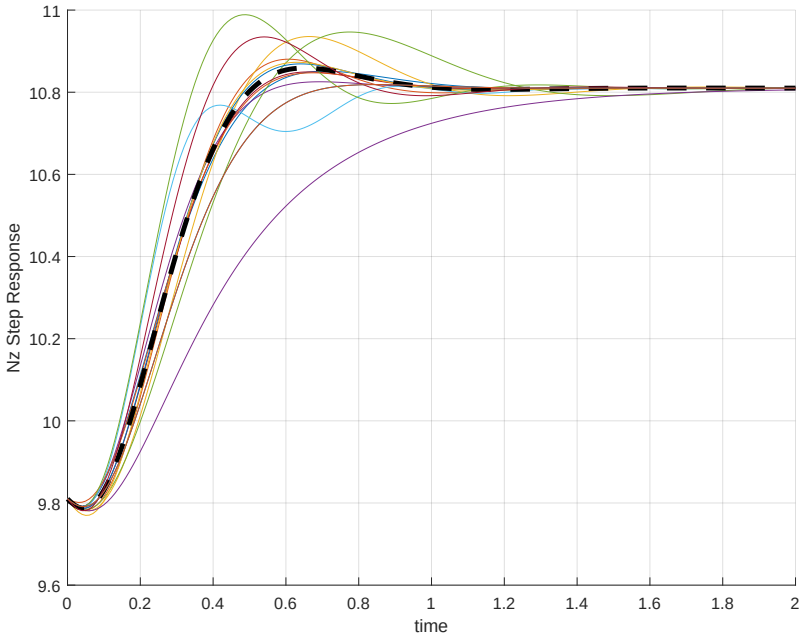

Figure 4.12: Robustness study - Nz time history step response

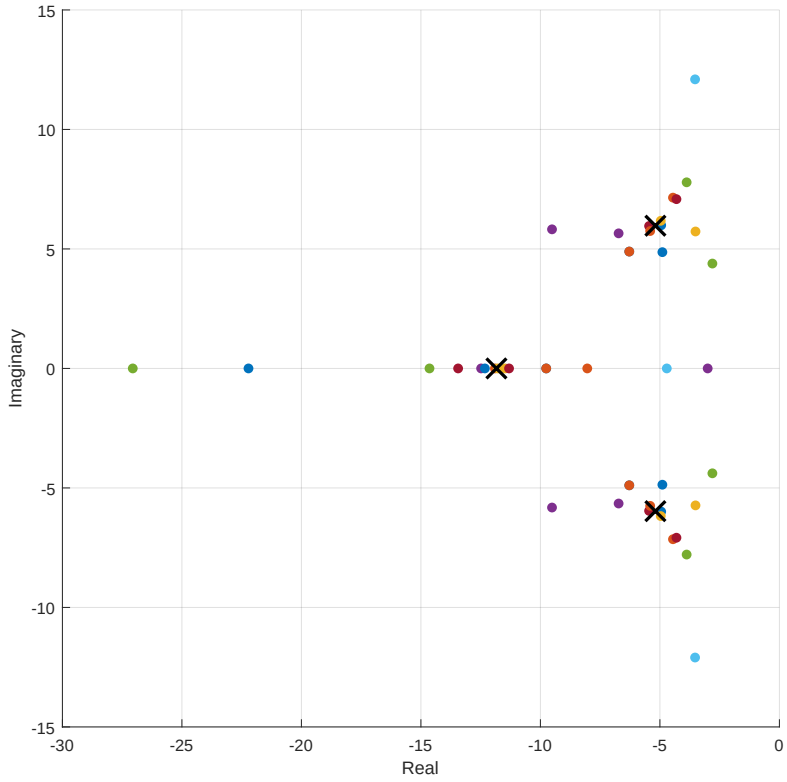

Figure 4.13: Longitudinal robustness study - root locus

Linear analysis supports the viability of the Biom T1 design in the longitudinal axis.

4.4.2 Lateral-Directional Control

Sideslip is the critical control state of the entire aircraft; there are minimal plant dynamics to invert in the controller, but also minimal control power among the two sets of control surfaces in yaw. The result is poor, but stable, closed-loop dynamics in yaw (note that roll control has good characteristics). Figure 4.14 shows the step response of sideslip.

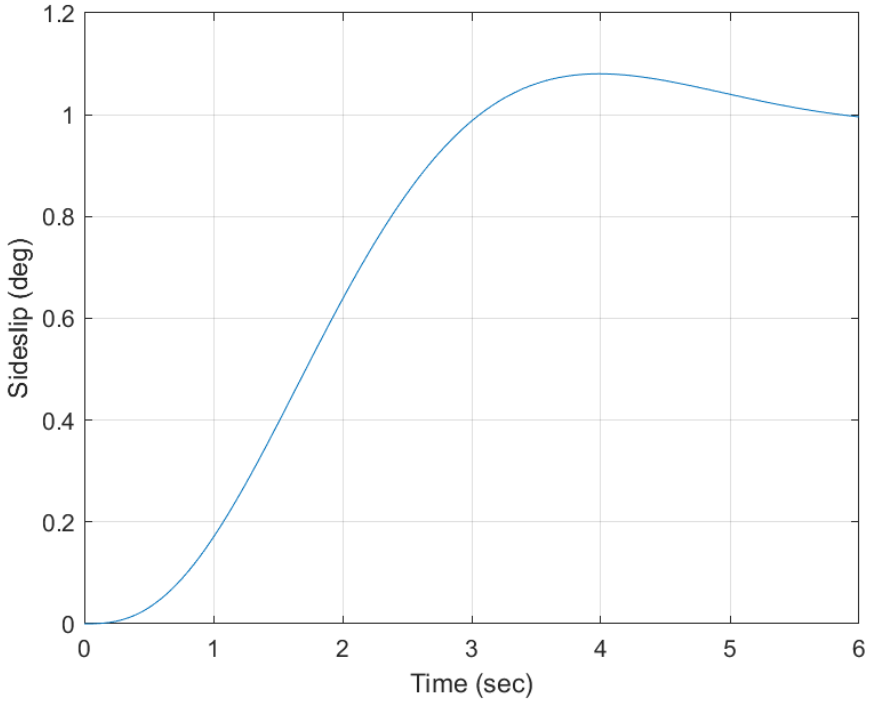

Figure 4.14: Sideslip Timehistory Step Response

Similar to the longitudinal axis, a linear robust study was done for lateral-directional control. The multi-input, multi-output nature of lateral-directional control made a strictly-eigen analysis more suitable than minimum singular values. The critical eigenvalue pair is the pair with the greatest (least negative) real component, and the value of this real component is the "eigenvalue margin" or "EV margin", and zeta is the damping ratio of this eigenvalue pair. Table 4.4 shows the response and margin to variations in the lateral-directional system.

Table 4.4: Variations in lateral-directional control to assess robustness

variation	overshoot	EV margin	zeta
BASELINE	8.04	-0.61	0.50
Ixx -50%	8.04	-0.61	0.50
Ixx +50%	8.04	-0.61	0.50
Izz -50%	5.37	-0.74	0.65
Izz +50%	12.3	-0.45	0.38
Lp -50%	8.07	-0.61	0.50
Lp +50%	8.01	-0.61	0.50
Lr -50%	8.14	-0.62	0.51
Lr +50%	7.95	-0.61	0.49
Lv -50%	8.05	-0.61	0.50
Lv +50%	8.04	-0.61	0.50
Np -50%	8.17	-0.61	0.50
Np +50%	7.92	-0.61	0.50
Nr -50%	8.04	-0.61	0.50
Nr +50%	8.04	-0.61	0.50
Nv eng	10.9	-0.56	0.48
Nv -50%	8.19	-0.61	0.50
Nv +50%	7.90	-0.62	0.50
Yv -50%	8.05	-0.61	0.50
Yv +50%	8.04	-0.61	0.50
cldi -50%	5.28	-0.75	0.66
cldi +50%	14.1	-0.39	0.34
cldo -50%	22.7	-0.21	0.21
cldo +50%	5.97	-0.73	0.62
cndi -50%	36.2	-0.09	0.09
cndi +50%	5.11	-0.73	0.67
cndo -50%	6.68	-0.69	0.57
cndo +50%	10.5	-0.50	0.41
m -50%	8.04	-0.61	0.50
m +50%	8.04	-0.61	0.50

Minimal degradation is observed with respect to most changes in parameters as can be seen from Table 4.4. Control power in particular, is very sensitive, as expected. Fifty percent reduction in $Cn_{\delta i}$ or $Cl_{\delta o}$ uses up most of the EV margin, greater yaw inertia also has poor margins. Other than these three cases, the system dynamics are robust against aerodynamic and mass property changes. Given that the magnitude of the uncertainty analysis is quite high at fifty-percent variation, the system still exhibits acceptable robustness.

In one particular case, an additional destabilizing yaw force was introduced to model the effect of the air-path (case "Nv eng"); unlike the control power variation cases, the dynamics were not noteworthy. Based on the max mass flow of the engine, N_v was estimated to be -0.005, for "Nv eng" $N_v = -0.02$. While directiional instability from inlets has caused issues for other flying wings, the lack of sweep makes the very front of the aircraft still quite close to the center of gravity, reducing the inlet's impact on yaw. Furthermore, this was testing of an unmodelled uncertainty against a baseline control system design; with a known source of instability such as this, including it in the design model originally would further improve robustness. Figure 4.15 shows the time history of step response for sideslip. Figure 4.16 shows the root locus for the lateral-directional robustness study and Fig. 4.17 shows the zoomed-in view of the root locus in Fig. 4.16.

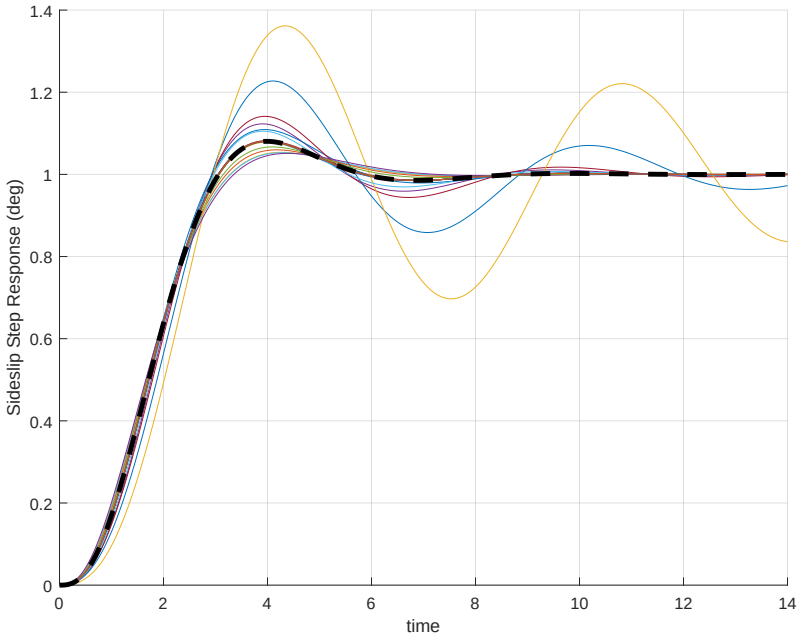

Figure 4.15: Robustness study - sideslip time history of step response

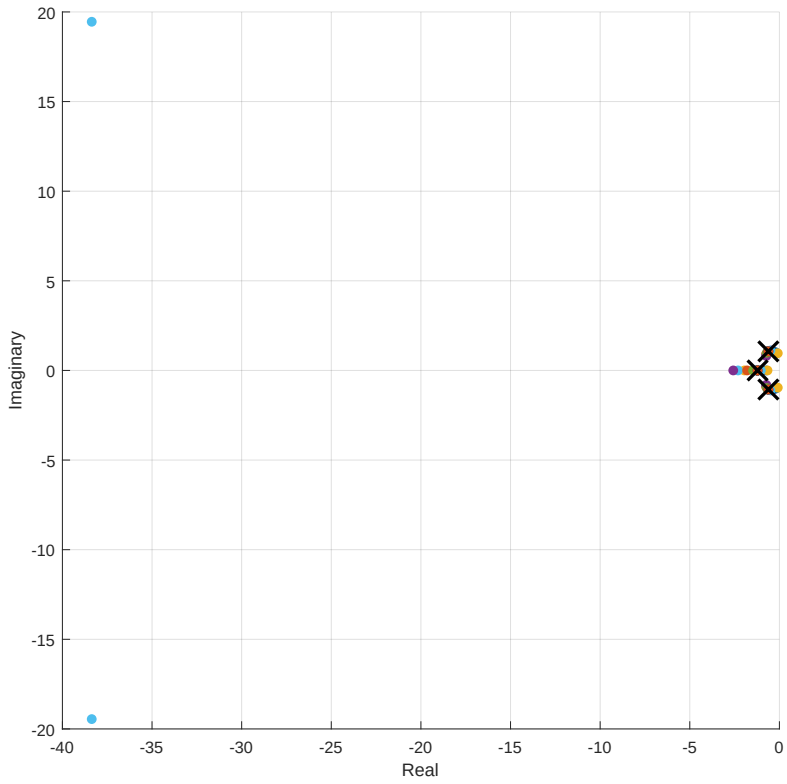

Figure 4.16: Lateral-directional robustness study - root locus

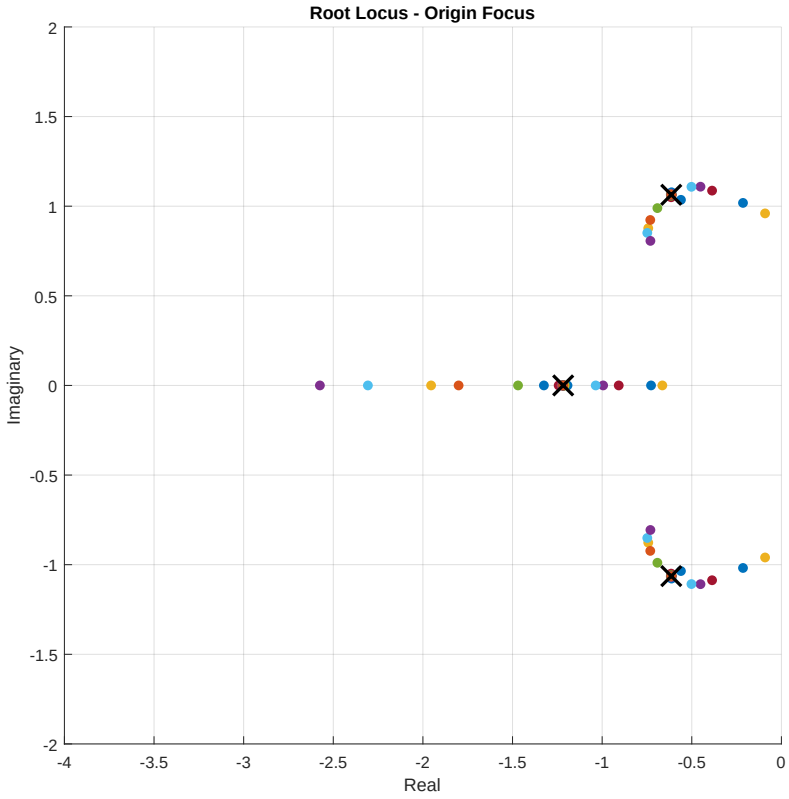

Figure 4.17: Lateral-directional robustness study - root locus, zoomed-in-view

4.4.3 Outeron Schedule

Positive collective outeron deflection is trailing edge up. Outside of a small deadzone, positive collective outeron is added with increasing angle of attack to unload the outeron, get closer to the bell-shape, and allow for larger differential outeron deflections before one of the surfaces stalls. Flight envelope is currently limited to trim AOA between -3 and 6 for controllability though this could be expanded with flight test. Within the small negative AOA range, outerons are rotated "into the flow" to reduce drag. Figure 4.18 shows the collective outeron command for various angles of attack and Fig. 4.19 shows the impact on the lift distribution of the outeron schedule in Fig. 4.18.

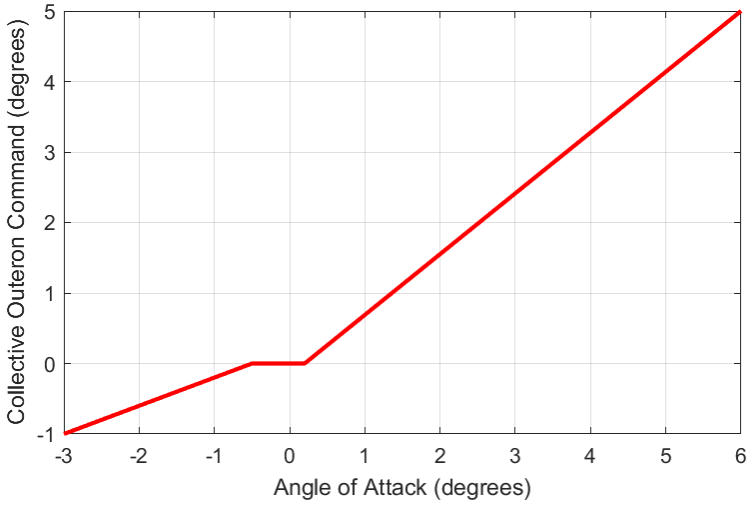

Figure 4.18: Outeron schedule

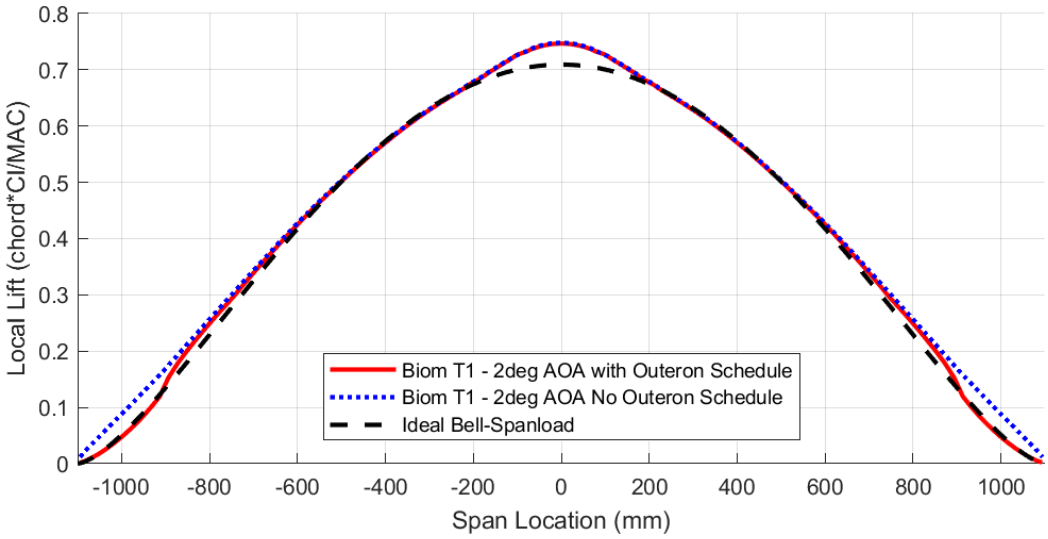

Figure 4.19: Impact of outeron schedule on lift distribution

Chapter 5

Biom T1 Flight Test Prototype

Results from flight test will be the subject of future research, but working toward the flight test goal illuminates unforeseen aspects of aircraft development when using a biom configuration that are relevant for design discussion at this point.

5.1 Sideslip Measurement

As identified in Section 4, observing sideslip might be problematic on a biom configuration and direct measurement is the lowest risk approach. A common measurement device is a weathervane-style design as shown in Fig. 5.1. When the aircraft begins to slip the freestream pushes against the side surface area of the vane and this deflection is measured by a rotational sensor [Karam(1975)].

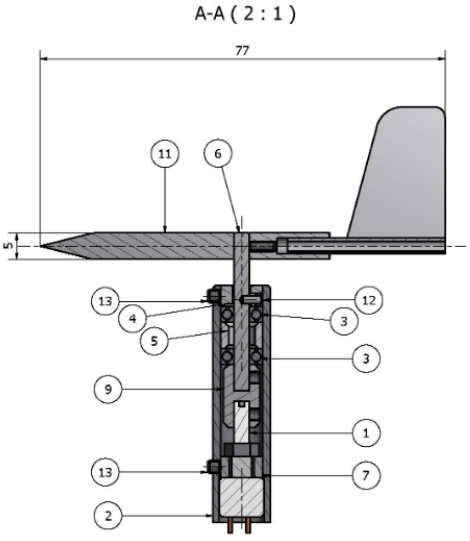

Figure 5.1: Traditional beta vane design [BasicAirData.eu(2014)].

Mounted above or below the centerline, this weather vane style should work well in the biom application as well. However the beta vane isn't suitable for all biom vehicles since some applications of this configuration place emphasis on no-vertical surfaces. As a solution in the general case, we have developed a specialized air-data probe instead. Generally packaged as a three-in-one alpha, beta, and total pressure probe, air data probes use multiple differential pressure sensors to detect angle of attack, angle of sideslip, and total pressure from at least five different pressure taps [Aeroprobe(2017)]. Commercially available beta and alpha probes were too large, heavy, and expensive to use on this project, so a smaller less complicated probe was considered.

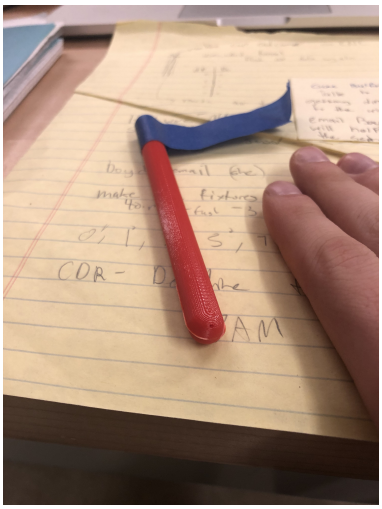

Figure 5.2: The 3D printed beta probe. (fingers are shown to describe the relative scale of the probe)

Two pressure taps from which differential pressure could be calculated were set 90 degrees apart on the forward hemisphere of beta probe. To estimate the pressure differential, the Cp slope was linearized surrounding the head of the probe [Anderson(2017)]. An Arduino Uno read pressure data from the Sensirion SDP31 Differential Pressure Sensor which specializes in small pressure differentials via an I2C datalink. Once all devices were incorporated, the pressure sensor and beta probe were tested in a low speed wind tunnel between zero and 24.1m/s at angles between zero and seven degrees. The wind tunnel was current limited via an electrical breaker, and was unable to achieve speeds higher than 24.1m/s (see Figs. 5.3a and 5.3b). This prevented testing to occur over the entire flight envelope from 0 to 40 m/s. Future testing is needed to confirm the beta probe can operate in velocities above 24m/s.

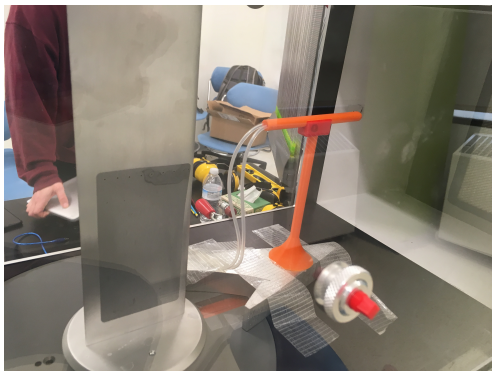

(a) Probe in the wind tunnel

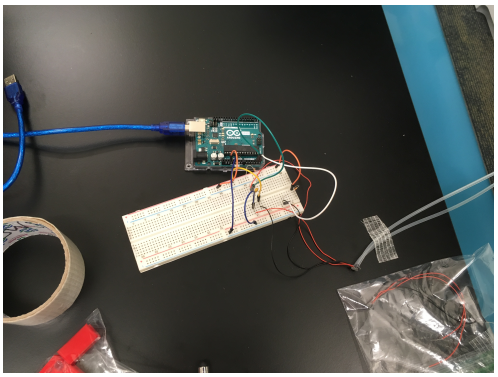

(b) Arduino and SDP32 setup

Figure 5.3: Wind tunnel setup for testing beta probe

Figures 5.4a - 5.4d are the results for slide slip angle vs differential pressure (DP) at constant velocities. Velocity data points were taken at 10, 15, 20, and 24m/s respectively in these figures. Side slip angle data points were taken at 7, 5, 2, 1, 0, -1, -2, -5, and -7 degrees. The zero degree sideslip angle was taken twice and the difference between data points at zero degrees deflection represents error within either the SDP31 sensor or the experimental setup. During wind tunnel testing, the SDP31 sensor was unable to read pressure differentials below 8m/s, and at 10m/s, the data for beta angles between zero and two degrees were within the margin of error for the sensor. Since dynamic pressure increases with the square of velocity, the differential pressure data fell outside of the range of possible sensor error at approximately 12m/s. The differential pressure data points at each velocity level fit to a linear relationship with all R2 values equal to or above 0.99.

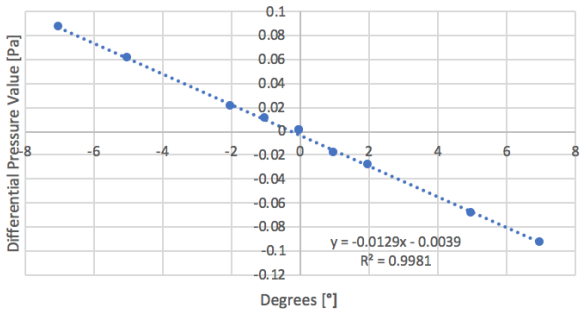

(a) DP at 10m/s

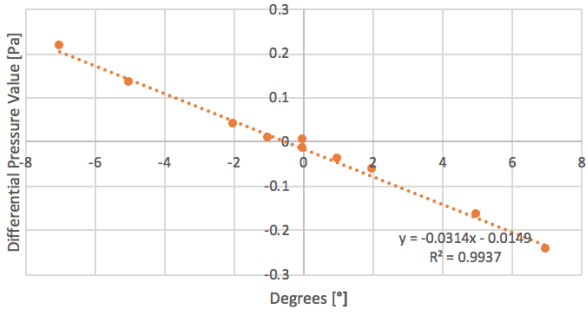

(b) DP at 15m/s

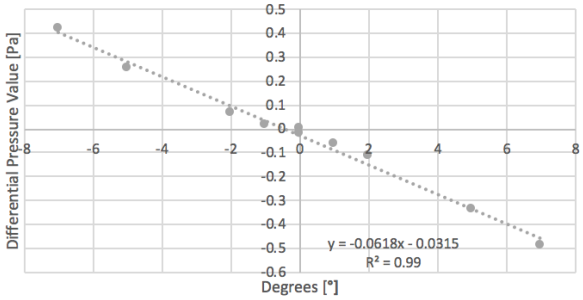

(c) DP at 20m/s

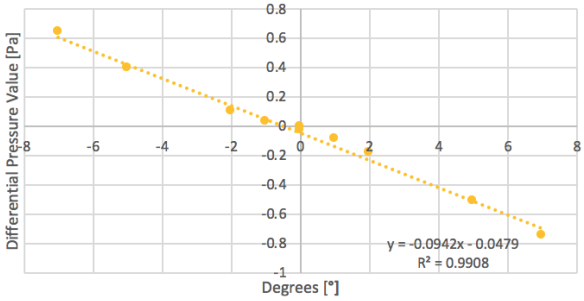

(d) DP at 24m/s

Figure 5.4: Differential pressure for beta at probe angles -7 through 7 degrees

The effects of dynamic pressure on differential pressure are easily visible when the pressure plots are overlaid as shown in Fig. 5.5. The increasing distance between data points at the same deflection angle confirm a non-linear relationship dependent on dynamic pressure.

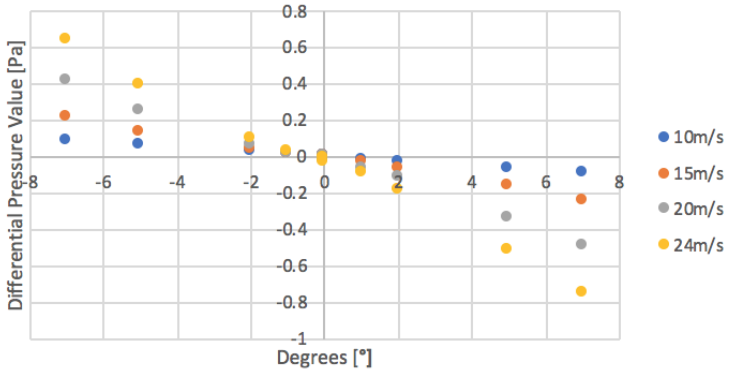

Figure 5.5: Overlaid pressure plots for beta probe measurements

Despite the high R2 value and the visible link with increasing dynamic pressure, the beta probe in its current form cannot adequately measure deflection angles at low velocities. Poor low-speed beta-probe performance set the minimum airspeed for our test vehicle at 15m/s. With this restriction, the beta probe works well for our application. A FADS could also be used, and is clearly of significance if developing a survivable design; however the biom configuration does not have good locations for flush pressure ports to measure sideslip. Other than the wingtips, the most lateral facing surface is the inflection point of the cosine extension region which is still relatively shallow on the leading edge. The airpath potentially is another source of lateral facing surface, though also not a good location due to measurement corruption by throttle state.

5.2 Guidance Laws

The slim profile, lack of sweep, and lack of dihedral, all lead to potential issues determining aircraft orientation when piloting via radio control line-of-sight. This establishes a requirement for a brightly colored orientation scheme and some kind of basic autonomy in the event that loss-of-orientation occurs.

For production purposes, autonomy is expected for a UAV, but testing generally starts line-of-sight and it is worth mentioning that basic autonomy should be tested as early as possible to mitigate this risk.

For the test program, a "return to home" reversionary mode has been developed where the flight management computer will take over control and fly the aircraft back to an orbit 250m above where it started. Initial attempts at developing this logic involved dividing the aircraft action into different regions so that if the aircraft is inside the pattern it would execute certain actions, if far away from the pattern a different set of actions and so on using a state machine to transition between these modes. This solution was becoming too complex and I sought a simple guidance law that would always result in smooth flight into the holding pattern without any conditional logic, the solution was a vector field and the result is shown in figure 5.6:

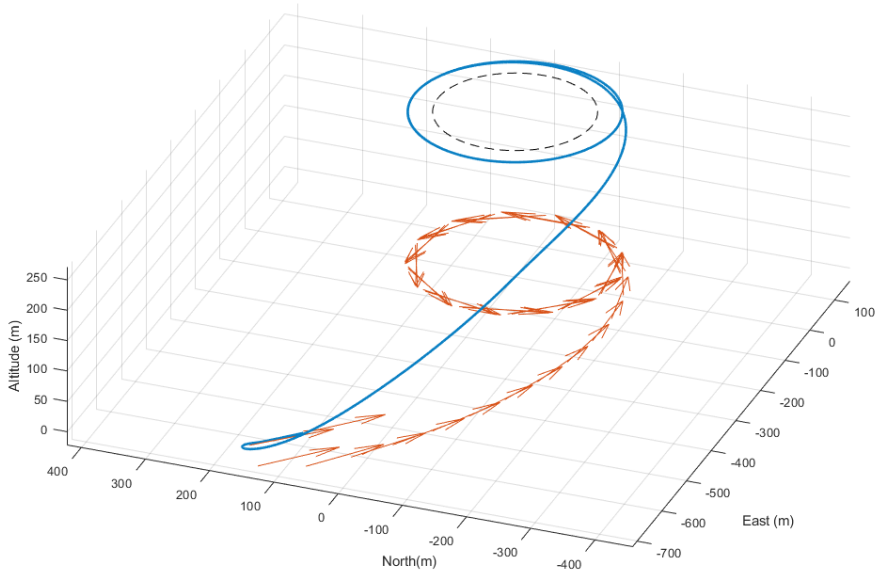

Figure 5.6: Return to home guidance - actual guidance laws piloting a model of Biom T1 in a Simulink 6dof simulation

Define point "C" as the center of the holding pattern (home location) and point "V" is the current vehicle location. The vector field is defined in polar coordinates (r,theta), where r is the radius error ($\mid CV \mid - pattern\_radius$) and theta is the angle between the "east" vector and the vector "CV".

Heading command is a combination of polar components $\dot{r}$ and $\dot{theta}$ defined in equations 5.2 and 5.2:

$$\dot{r} = -ar \tag{5.1}$$

$$\dot{theta} = -b \tag{5.2}$$

where a is the radius tracking gain, and b is equal to the target groundspeed divided by the pattern radius, however ultimately only the ratio of a and b really matters since after this polar vector is calculated, only the direction is used in the form of the heading command.

In this formulation, if we assume sufficiently fast flight control tracking of this heading command, we can use state dynamics to determine stability. In this case verifying stability is trivial, particularly since the polar components are independent. The radius differential equation on it's own is stable by inspection or by lyapunov function r^2. On the other hand, $\dot{\theta}$ doesn't even have dynamics per-se, but the heading becomes defined by $\dot{\theta}$ as $\dot{r}$ is driven to zero. This gives confidence that independent of the starting aircraft location and heading it will smoothly transition to this holding pattern.

Altitude guidance is treated independently and simply produces a flight path angle command as a function of altitude error, the flight path angle command is limited such that most of the time the aircraft flies up against the climb/dive limits until the aircraft is close to the target altitude where the proportional behavior becomes apparent and smooths out this transition.

All guidance logic discussed up to this point is implemented in the "trajectory determination" subsystem and it's commands drive the "trajectory tracking" subsystem which contains the outer loops for steering and axial control. Control laws implemented in the trajectory tracking subsystem are relatively standard and will not be discussed.

Timehistories of the test case in figure 5.6 are shown in Appendix A, this test case initializes fast, far away, low altitude, pointing away and flying in a clockwise sense relative to the home location. Guidance overcomes all of these adverse conditions and smoothly enters the holding pattern in the proper direction.

5.3 VMS Development

For a simple, small research platform, we developed a simplex architecture for a pixhawk 4 running at 250Hz for flight control and 50Hz for everything else. The OFP (operational flight program) was used on a small foam "iron bird" platform for actuator characterization testing and verified the input processing and mode selection logic. The guidance subsystem was able to be verified through simulation but unfortunately flight control was not.

The DS95i elevator servos require a 560Hz narrow-width PWM signal so the "I/O" CPU was configured to run these servos while the FMU CPU runs all other PWM outputs including the four lateral-directional servos and one electronic speed control.

The Pixhawk takes air data from two booms (one for sideslip, one for airspeed) using I2C bus communication. Standard pixhawk modules are used for power, GPS, and telemetry.

VMS software is produced using the Simulink PX4 support package; custom VMS software is entirely autocoded and loaded onto the pixhawk using simulink. This tool process was helpful in running in external mode to capture actuator data and troubleshoot the OFP mode selection logic, we were also able to demonstrate running the OFP in a hardware in the loop simulation where the pilot was able to hand control back and forth to the guidance reversionary mode.

Chapter 6

Application

6.1 Stacking

When stored in a larger space, each fully-assembled Biom T1 uses up very little volume; Biom configurations tessellate well in three-dimensional space. In particular, they stack well vertically since there are no vertical aspects in the design. For instance, search and rescue operations may launch UAVs from a van deployed to the location of the crisis. Numerous biom-type aircraft could be stored in the van and launched very quickly since they require no assembly or re-configuring from their "tight-stacked" configuration to their "flight" configuration.

Similarly, for military applications, multiple biom UAVs could be tightly packed and shipped to various military bases to have on standby for quick deployment in intelligence, surveillance, and reconnaissance operations.

Some planetary science proposals involve sending gliders to other bodies in the solar system. For sending multiple gliders to an outer-system body such as Titan, payload volume is very limited and is very valuable. More gliders of a biom configuration could be deployed on such a mission than other aircraft configurations, and without any risky deployments or re-configuring.

6.2 Survivability

Tailless flying wings are used in military intelligence, surveillance, and reconnaissance (ISR) applications where it is advantageous that the aircraft is not easily detectable or easily engaged.

Lacking vertical tails, aerodynamic yaw moment in these configurations is generated by differential drag produced by split ailerons or by a "crow mix" between inner and outer ailerons. Crow mix is where inner and outeron ailerons on one side of the aircraft produce opposite rolling moment which cancel each other out but produce a yawing moment due the additional drag from control deflection.

In a split-aileron configuration, one must bias the surfaces into a pre-deflected state in order to use the full control power of all four actuators at once: two can "close" to reduce drag on one side and two can "open" to increase drag on the opposing side. Without biasing, two actuators must move twice as fast to get the same transient yaw response. The actual impact to actuator requirement may be higher bandwidth, higher max rate, or some combination, but the key point is that there is a tradeoff between biasing and actuator requirements in a split-aileron configuration.

Crow-mix is similar to split-aileron, although crow-mix is generally not biased since this is detrimental to the lift distribution. Without any biasing, only two of the surfaces can be used at once, still impacting actuator requirements.

In contrast, the lateral-directional control scheme used on Biom T1 does not have this tradeoff: all four actuators involved with yaw motion (both innerons and both outerons) can act appropriately without biasing or adversely impacting the lift distribution in steady state. Furthermore, the control itself is more efficient in terms of lower drag per yawing moment.

This lateral-directional control scheme, by itself (though contingent on also using a bell-shaped-spanload) could be employed to improve tailless flying-wings in general. However, there are additional advantages the Biom configuration as a whole offers. Clearly the design under study thus far is not a survivable instance, but the general configuration allows survivable designs.

The most notable advantage to a Biom configuration is that the forward facing profile can be one contiguous straight line as shown in Fig. 6.1.

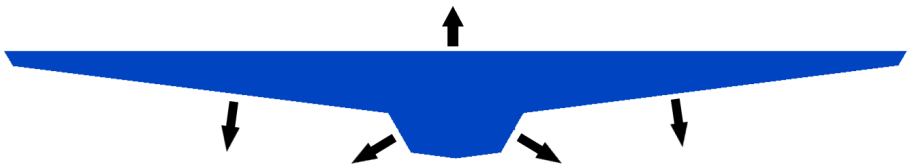

Figure 6.1: Survivable Biom geometry

This presents only one direction of major radar return when approaching a threat (directly forward), greatly simplifying mission planning for avoiding known threats.

6.3 Performance

Using the simplified Breguet range equation:

$$Range = \frac{\frac{L}{D}V_{cruise}}{g * SFC} ln\left(\frac{W_{initial}}{W_{final}}\right), \tag{6.1}$$

the range of the Biom T1 design with a turbine engine installed would be about 300km with the following assumptions:

- specific fuel consumption of 0.19 kg/(N hr)
- 1.9kg of fuel
- 1.9kg airframe
- cruising speed of 25m/s
- L/D of 10 at that condition

The specific fuel consumption is based on a jetcat P-20SX, the fuel weight is based on what can fit given the low internal payload volume, and the L/D is a conservative estimate based on the capabilities of existing technology at these sizes and flight conditions.

With the heavy emphasis on control analysis, panel methods were selected for quick iteration on geometries including control surfaces. Unfortunately this precludes any serious assessment of whether this configuration offers a performance improvement over traditionally configured aircraft. The advantages of not having a fuselage or tail and de-sweeping the wing is offset by the aerodynamic penalties of using reflex airfoils and a bell-shaped lift distribution (while great for reducing induced drag, the bell spanload has sub-optimal viscous drag [Wroblewski(2016)]) and we have no data to suggest if the tradeoff is worthwhile from a purely aerodynamic performance standpoint.

Chapter 7

Conclusions

Based on this study, the following conclusions can be drawn. Using a bell-shaped-spanload, proverse yaw from outeron deflections is the result of increased induced thrust inboard of the outeron itself. On the same vehicle proverse yaw and adverse yaw can be achieved using control surfaces in different locations relative to the mid-span vortex, verifying that arbitrary roll-yaw combinations are possible within a parallelogram-shaped control space. A straight-flying wing utilizing this lateral-directional control scheme is feasible, providing a platform for further study in avian flight and morphing geometry. Such a configuration is suitable for long-range or high-endurance platforms with low-volume payloads. Future work should include flight test of the biom vehicle, application of compliant structures, and variable sweep as a primary flight control, perhaps only in the outer portion of the wing.

Appendix A

Guidance Test Case Timehistories

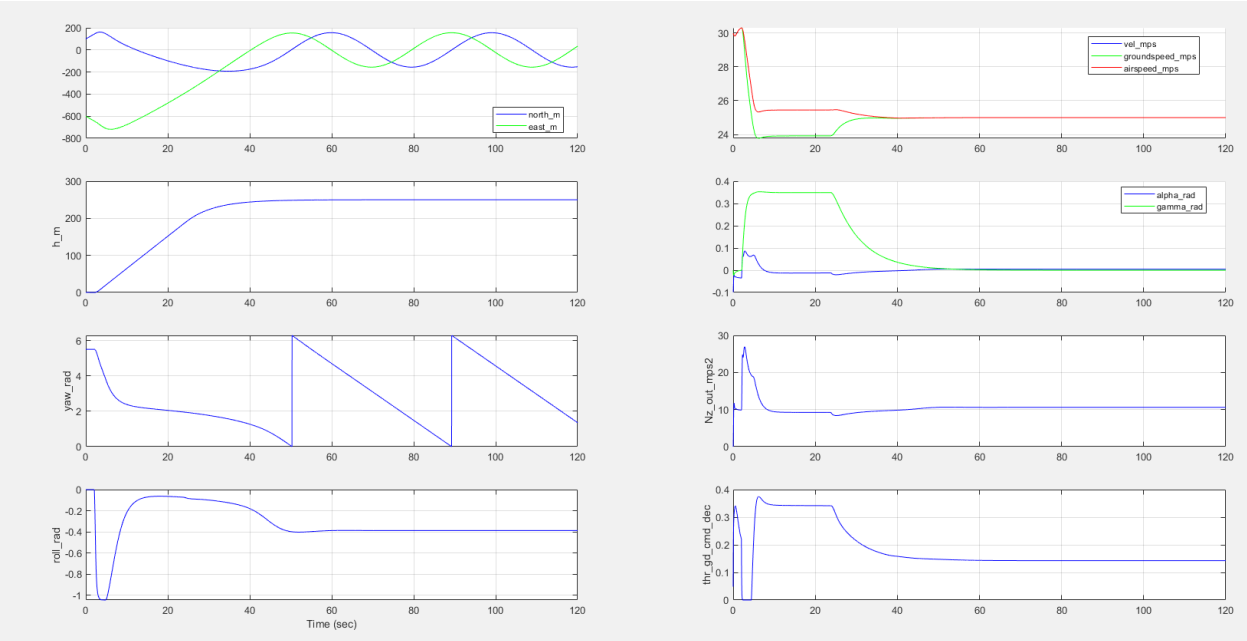

Figure A.1: General Signals

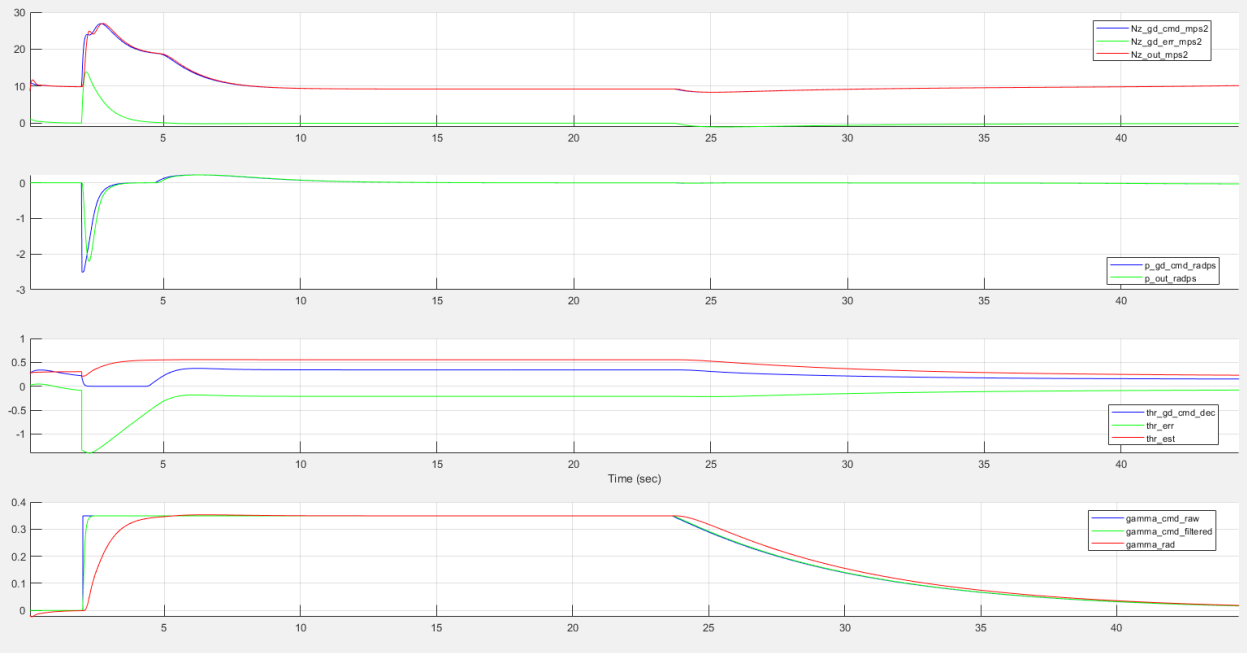

Figure A.2: Trajectory Tracking

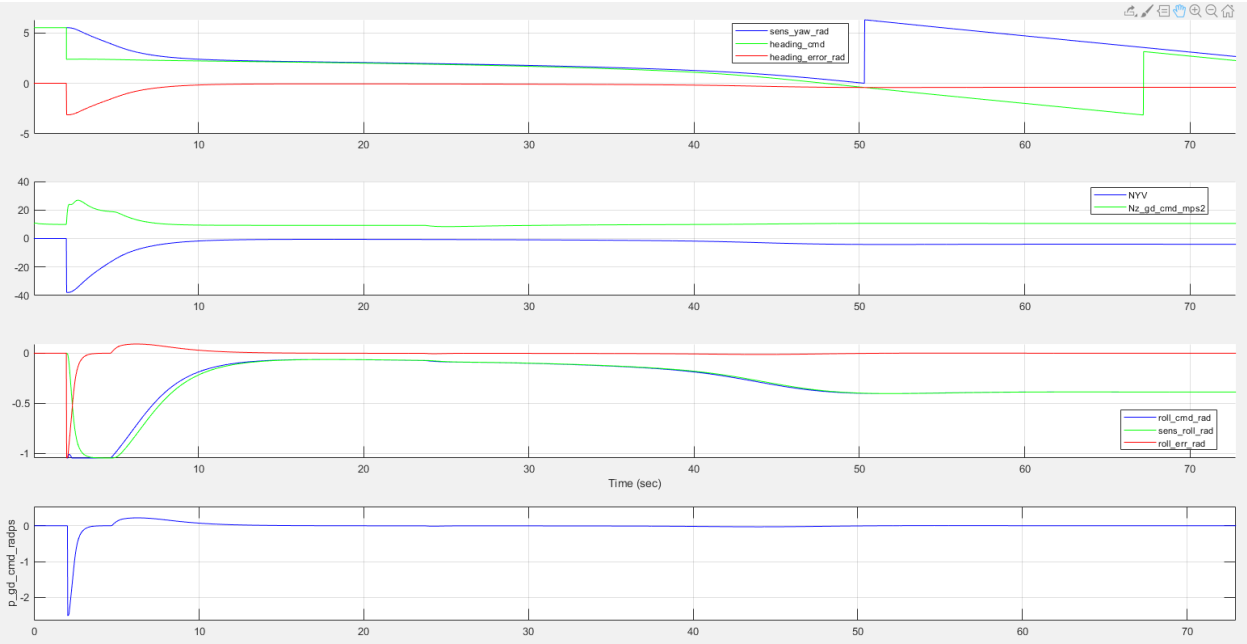

Figure A.3: Trajectory Tracking Cont.

Appendix B

High Level Block Diagrams

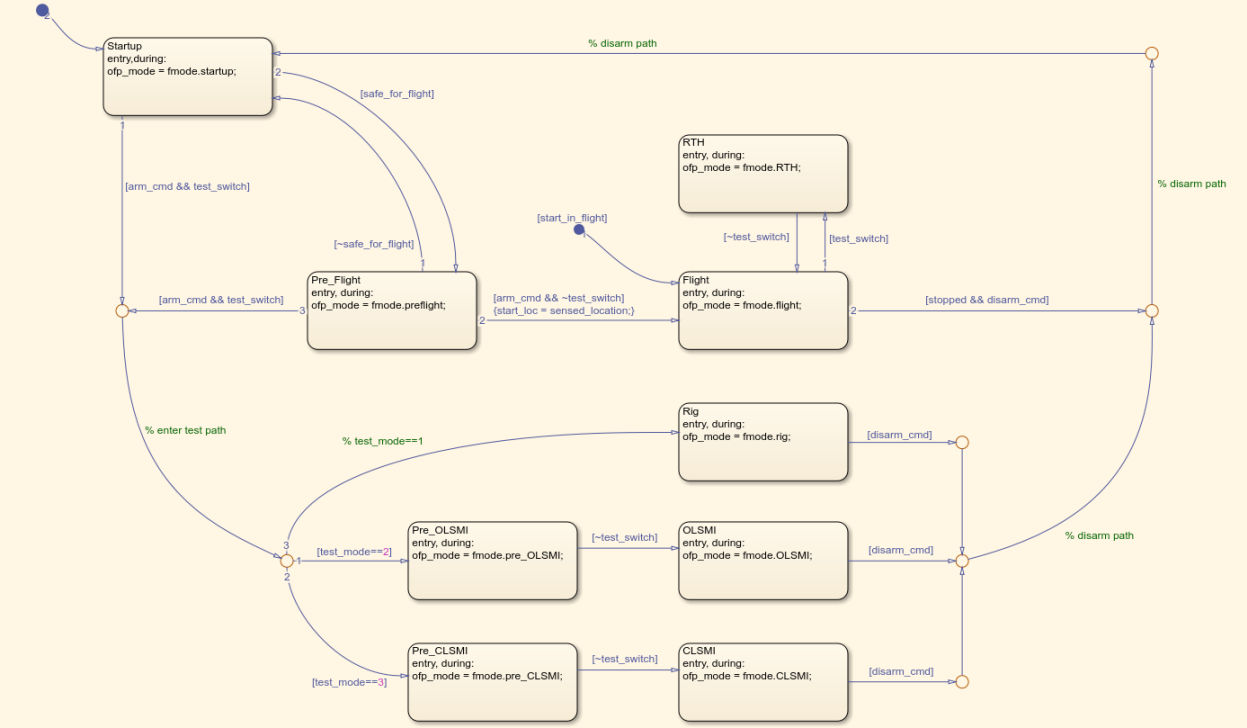

Figure B.1: OFP Mode Logic

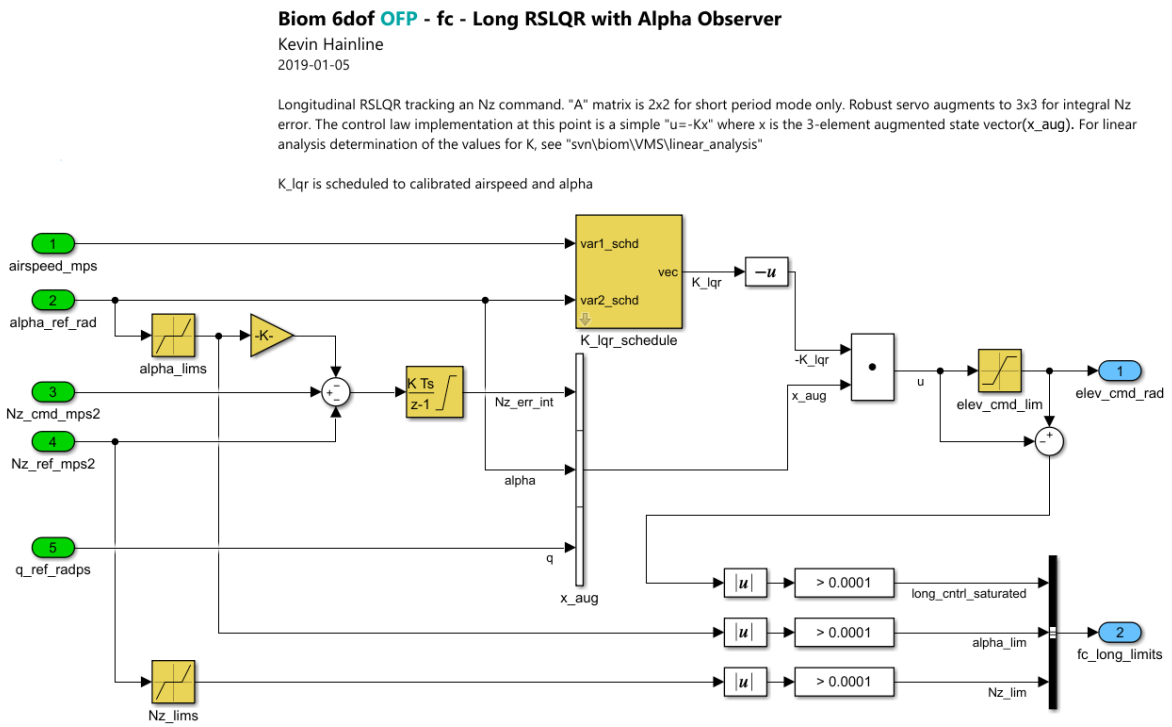

Figure B.2: Longitudinal Control Law Implementation

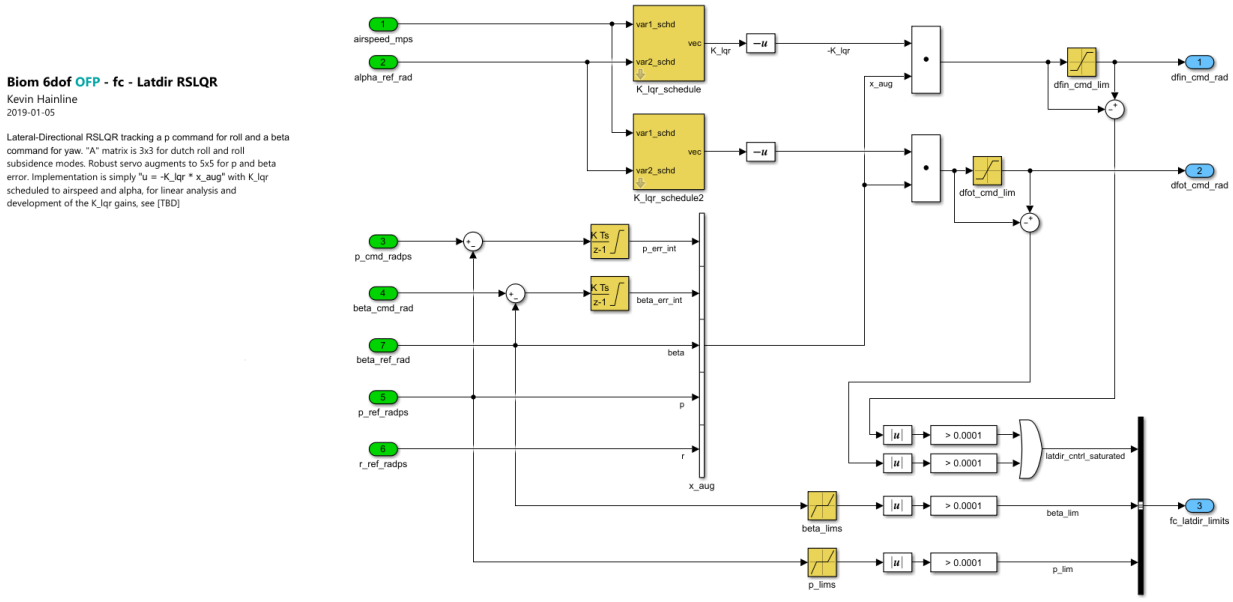

Figure B.3: Lateral-Directional Control Law Implementation

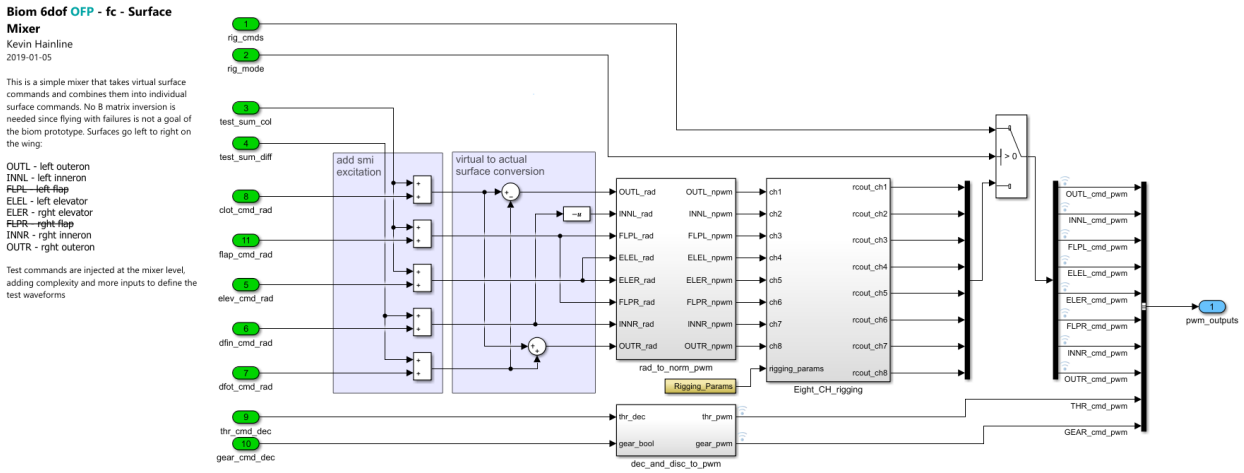

Figure B.4: Mixer Implementation

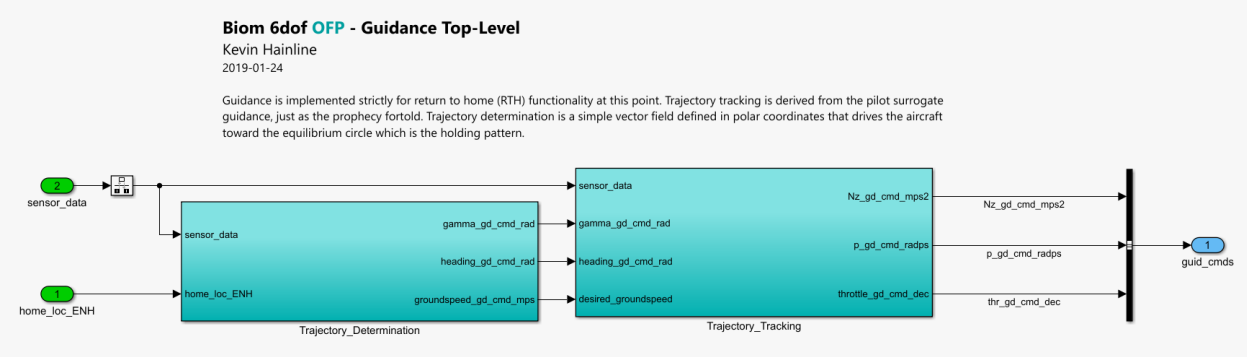

Figure B.5: Guidance Top-Level

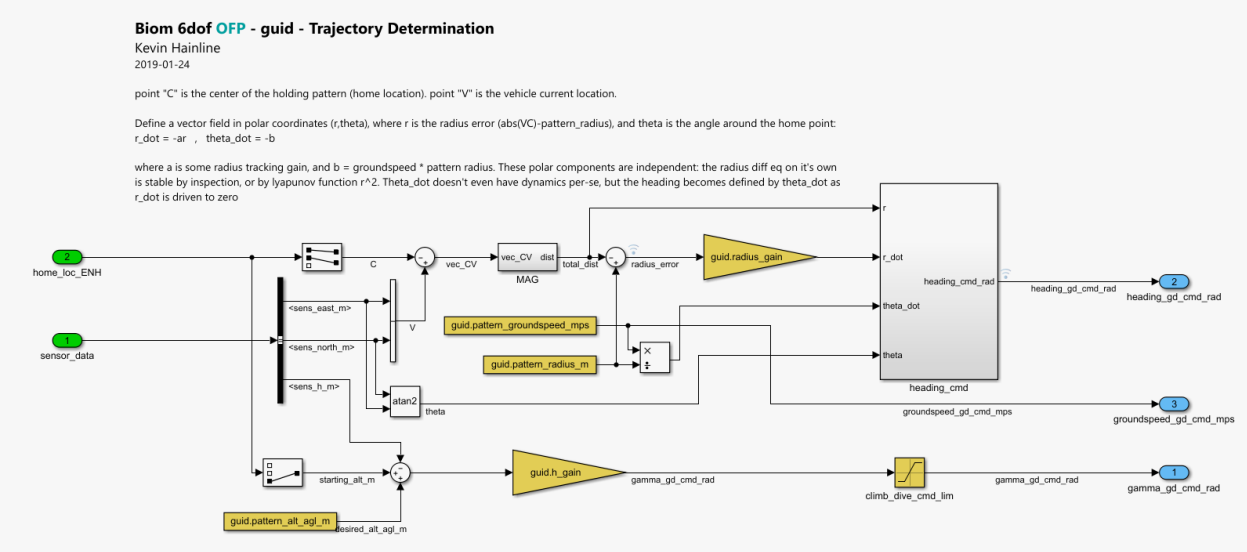

Figure B.6: Trajectory Determination

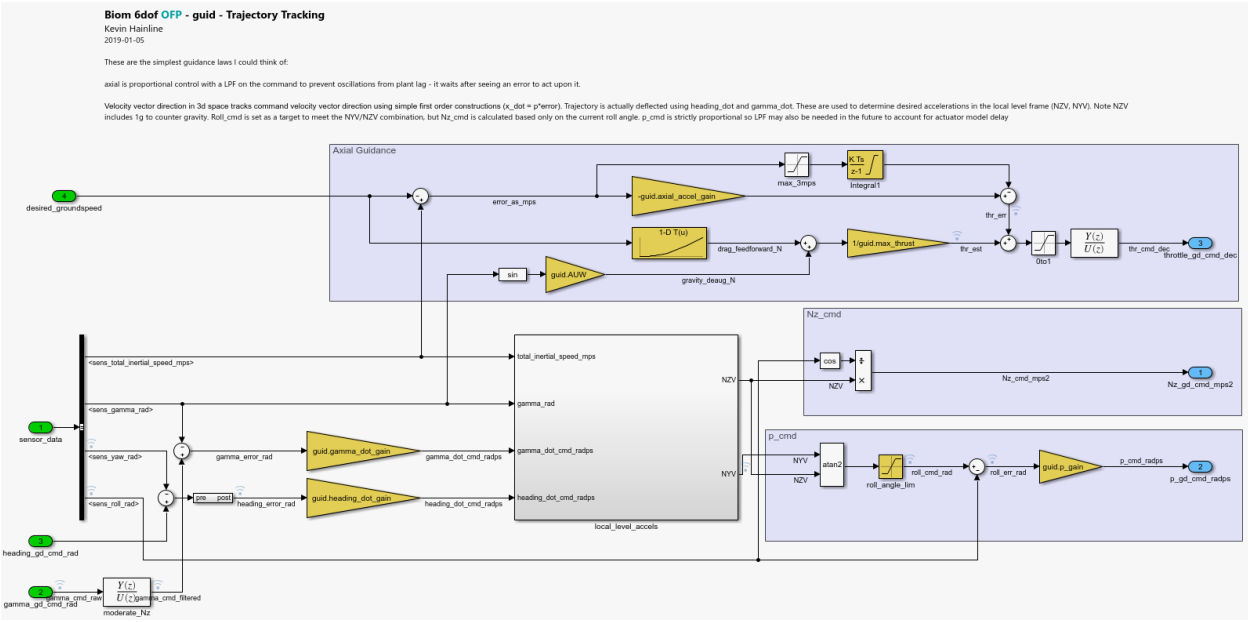

Figure B.7: Trajectory Tracking

Appendix C

Linear Analysis Data

Table C.1: Full Table Data Longitudinal Robustness

name	undershoot	overshoot	RDu_GMp	SRu_GMp	RDu_GMm	SRu_GMm	SRu_PM
Iyy_m30	1.8	4.1	77.953	5.20	-6.02	-14.94	48.47
Iyy_p30	2.7	7.0	18.301	4.55	-5.47	-10.15	40.32
Mde_m30	2.9	12.6	20.936	4.56	-5.62	-10.20	40.43
Mde_p30	1.9	1.5	90.381	5.13	-6.02	-14.21	47.49
Mq_p100	2.5	13.7	77.729	4.90	-6.02	-12.35	44.59
Mq_zero	2.1	0.5	6.9354	3.14	-3.80	-4.973	25.17
Mw_m50	2.3	3.9	127.93	5.00	-6.02	-13.12	45.86
Mw_p50	2.3	5.9	127.21	4.83	-6.02	-11.88	43.76
Zde_m50	0.9	3.7	104.30	4.98	-6.02	-12.94	45.57
Zde_p50	4.0	6.3	44.381	4.85	-5.99	-12.00	43.99
Zw_m50	2.9	-0.4	131.31	5.38	-6.02	-17.03	50.88
Zw_p50	2.0	17.9	23.201	4.46	-5.71	-9.700	39.30
baseline	2.3	4.9	127.56	4.92	-6.02	-12.48	44.81
m_m20	2.9	12.5	31.641	4.65	-5.90	-10.72	41.52
m_p20	1.9	0.9	112.99	5.09	-6.02	-13.87	47.00
m_p20	1.9	0.9	112.99	5.09	-6.02	-13.87	47.00

References

[Dvorak(2016)] Dvorak, R., "Aerodynamics of Bird Flight," *EPJ Web of Conferences*, Vol. 114, No. 01001, 2016.

[Bowers and Murillo(2016)] Bowers, A. H., and Murillo, O. J., "On Wings of the Minimum Induced Drag: Spanload Implications for Aircraft and Birds," *NASA/TP-2016-219072*, 2016.

[Silvestro Barbarino(2011)] Silvestro Barbarino, e. a., "A Review of Morphing Aircraft," *Journal of Intelligent Material Systems and Structures*, Vol. 22, 2011, p. 823–877. doi: 10.1177/1045389X11414084.

[Gilbert(1981)] Gilbert, W. W., "Mission Adaptive Wing System for Tactical Aircraft," *Journal of Aircraft*, Vol. 18, No. 7, 1981, pp. 597–602. doi:10.2514/3.57533.

[Marks et al.(2015)Marks, Zientarski, Culler, Hagen, Smyers, and Joo] Marks, C. R., Zientarski, L., Culler, A. J., Hagen, B., Smyers, B. M., and Joo, J. J., "A Review of Morphing Aircraft," 2015. doi:10.2514/6.2015-1051.

[Prandtl(1933)] Prandtl, L., "On Wings with Minimum Induced Drag," *Zeitschrift Flugtechnik und Motorluftschiffahrt*, Vol. 24, 1933.

[R.T.Jones(1950)] R.T.Jones, "The Spanwise Distribution of Lift for Minimum Induced Drag of Wings Having a Given Lift and a Given Bending Moment," *NASA Tech Note No. 2249*, 1950.

[Klein and Viswanathan(1975)] Klein, A., and Viswanathan, S., "Approximate Solution for Minimum induced Drag of Wings with a Given Structural Weight," *AIAA Journal of Aircraft*, Vol. 12, No. 2, 1975.

[Wroblewski(2016)] Wroblewski, G., "Prediction and Experimental Evaluation of Planar Wing Spanloads for Minimum Drag," *University of Illinois at Urbana-Champaign M.S. Thesis Paper*, 2016.

[Iglesias and Mason(2001)] Iglesias, S., and Mason, W. H., "Optimum Spanloads Incorporating Wing Structural Weight," *AIAA, Aircraft, Technology Integration, and Operations Forum*, AIAA, Los Angeles,CA,USA, 2001. doi:10.2514/6.2001-5234.

[Munk(1923)] *The Minimum Induced Drag of Aerofoils*, NACA Report No. 121, 1923.

[Cohen(1945)] *A Method for Determining the Camber and Twist of a Surface to Support a Given Distribution of Lift, with Applications to the Load Over a Sweptback Wing*, NACA Report No. 826, 1945.

[Kuhlman(2003)] Kuhlman, B. . B., "On The Wing, Twist Distributions for Swept Wings," *R/C Soaring Digest*, Vol. 20, No. 6, 2003, p. 6.

[Karam(1975)] Karam, J. T., "Dynamic behavior of Angle-of-Attack Vane Assemblies," *Journal of Aircraft*, Vol. 12, No. 3, 1975, pp. 190–192. doi:10.2514/3.44432.

[BasicAirData.eu(2014)] "Beta Vane Diagram," 2014. URL `https://www.basicairdata.eu/knowledge- center/design/angle-of-attack-vane/`.

[Aeroprobe(2017)] Aeroprobe, "Air Data Probe," 2017. URL `http://www.aeroprobe.com/air-data-probe/`.

[Anderson(2017)] Anderson, J., *Fundamentals of Aerodynamics*, 6$^{\text{th}}$ ed., McGraw-Hill Education, New York, NY, 2017.